(12) **LEVEL** II

AD-E300 358

DNA 4611F

CENTRIFUGE SIMULATION OF LARGE YIELD CRATERING EVENTS

Pacifica Technology
P.O. Box 148
Del Mar, California 92014

30 December 1977

Final Report for Period 1 February 1977—30 December 1977

CONTRACT No. DNA 001-77-C-0116

APPROVED FOR PUBLIC RELEASE;
DISTRIBUTION UNLIMITED.

D D C

RECEIVED

NOV 22 1978

B

Prepared for

Director
DEFENSE NUCLEAR AGENCY
Washington, D. C. 20305

78 10 04 012

UNCLASSIFIED
SECURITY CLASSIFICATION OF THIS PAGE (When Data Entered)

REPORT DOCUMENTATION PAGE		READ INSTRUCTIONS BEFORE COMPLETING FORM
1. REPORT NUMBER DNA 4611F	2. GOVT ACCESSION NO.	3. RECIPIENT'S CATALOG NUMBER
4. TITLE (and Subtitle) CENTRIFUGE SIMULATION OF LARGE YIELD CRATERING EVENTS		5. TYPE OF REPORT & PERIOD COVERED Final Report. 1 Feb 77 — 30 Dec 77
		6. PERFORMING ORG. REPORT NUMBER PT-U77-0161
7. AUTHOR(s) R. T. Allen R. L. Bjork E. S. Gaffney		8. CONTRACT OR GRANT NUMBER(s) DNA 001-77-C-0116
9. PERFORMING ORGANIZATION NAME AND ADDRESS Pacifica Technology P.O. Box 148 Del Mar, California 92014		10. PROGRAM ELEMENT PROJECT, TASK AREA & WORK UNIT NUMBERS Subtask H35HAXSX355-22
11. CONTROLLING OFFICE NAME AND ADDRESS Director Defense Nuclear Agency Washington, D.C. 20305		12. REPORT DATE 30 December 1977
		13. NUMBER OF PAGES 86
14. MONITORING AGENCY NAME & ADDRESS(if different from Controlling Office)		15. SECURITY CLASS. (of this report) UNCLASSIFIED
		15a. DECLASSIFICATION DOWNGRADING SCHEDULE
16. DISTRIBUTION STATEMENT (of this Report) Approved for public release; distribution unlimited.		
17. DISTRIBUTION STATEMENT (of the abstract entered in Block 20, if different from Report)		
18. SUPPLEMENTARY NOTES This work sponsored by the Defense Nuclear Agency under RDT&E RMSS Code B344077462 H35HAXSX35522 H2590D.		
19. KEY WORDS (Continue on reverse side if necessary and identify by block number) Crater Simulation PETN JOHNIE BOY Centrifuge		
20. ABSTRACT (Continue on reverse side if necessary and identify by block number) Gravity plays an increasingly important role in cratering and ground motion for larger yield events. The effects of gravity may be accounted for by conducting experiments in a centrifuge. A review of previous applications of centrifuge testing to cratering and related problems is presented. The development of a high explosive charge equivalence for the JOHNIE BOY event is discussed. Sensitivity studies and areas of uncertainty in this simulation charge design are given. Experimental tests of this charge equivalence are presented.		

DD $\begin{smallmatrix} \text{FORM} \\ \text{1 JAN 73} \end{smallmatrix}$ 1473 EDITION OF 1 NOV 65 IS OBSOLETE

UNCLASSIFIED
SECURITY CLASSIFICATION OF THIS PAGE (When Data Entered)

20. ABSTRACT (Continued)

The results of centrifuge testing are analyzed within the context of other cratering data from high explosive and nuclear events. Equations for predicting crater volume in alluvium and coral sand for both high explosive and nuclear sources are given. Crater shape is found to be a function only of lithology and scaled height of burst except for the high yield Pacific Proving Ground events. Deviations of observed crater volumes and shapes from the general trend of the data show a strong positive correlation.

TABLE OF CONTENTS

LIST OF ILLUSTRATIONS

LIST OF TABLES

1. INTRODUCTION AND SUMMARY

By dimensional analysis, one can establish that gravity plays an increasingly important role in cratering and ground motion for larger yield events, and that the effects of material strength are relatively less important at larger yields. It has long been recognized[1] that these considerations prevent scaling high explosive phenomena up to multi-kiloton yields and higher by the so-called hydrodynamic scaling ($W^{1/3}$).

The data base confirms the inapplicability of scaling crater dimensions by $W^{1/3}$. A considerable amount of research[2-11] has been devoted to develop scaling laws using other yield exponents. Many of these research efforts have specifically recognized the influence of gravity. Scaling by means of a yield exponent remains controversial[12], however, and it is highly desirable to be able to simulate large yield events in various media by an inexpensive means. As discussed in Section 2, the effects of gravity may be taken into consideration by conducting the experiment in a centrifuge. If the linear dimensions of an experiment are scaled down by the same factor by which the gravitational acceleration is scaled up, dynamic similitude is preserved. That is, if one uses the same material in both experiments, its material properties scale correctly as long as rate effects are unimportant. This comment applies to the material properties of the geologic medium, the high explosive and air. Thus, both the direct-induced and the airblast-induced ground motions scale properly in a centrifuge experiment. It can be shown that the yield scales as the cube of the experimental dimension, so that at 500 g's one gram of HE simulates the effects of 125 tons of the same HE.

The work described in this report was undertaken to provide theoretical support and analysis for an experimental program conducted by R. M. Schmidt of the Boeing Company under separate contract to the Defense Nuclear Agency. We should point out that the final analysis of these test results will be given by Schmidt in a separate report, and the results as discussed here are preliminary. It is not expected that our conclusions will be modified by additional data reduction.

A brief review of previous applications of centrifuge testing to cratering and related problems is given in Section 2. The development of a high explosive charge equivalence for the JOHNIE BOY event is discussed in Section 3. This charge was incorporated into the Boeing test matrix. Finally in Section 4, the results of the Boeing tests are discussed within the context of the results of other cratering events. The program objectives and the conclusions and recommendations which we feel have resulted from this effort are presented in the remainder of this section.

1.1   PROGRAM OBJECTIVES

The ultimate goal of centrifuge simulation of large yield events is the reproduction of the crater results observed on the nuclear events at the Pacific Proving Ground[13], and hopefully some experimental guidance for resolution of the differences[14] between empirical predictions and detailed finite difference calculations of craters from nuclear surface bursts. Funding limitations imposed more modest objectives on this first effort. The Boeing test matrix was limited to twelve events. The first series of six shots was conducted in Ottawa sand so that extensive testing performed by Piekutowski[15] could be used as a tie point to results at normal gravity. The objectives of these first six tests were:

- Determine reproducibility
- Quantify centrifuge scaling*
- Explore effects of particle size variation.

A Program Review Meeting was held at the end of this phase of testing. It was the consensus of the group** that while the objectives of this first series of shots had been achieved quite well, Ottawa sand did not represent a satisfactory material for simulation of events in desert alluvium. Field material, with the larger particles removed, was provided to Boeing by R. W. Henny of the Air Force Weapons Laboratory. The last six tests were conducted in this medium and devoted to the following objectives:

- Verify reproducibility and quantify centrifuge scaling
  in this new material

*See Section 2.2.3
**Included representatives of DNA/SPSS, AFWL, PacTech and Boeing.

6

- Test the predicted JOHNIE BOY simulation charge

- Explore the sensitivity of the simulation charge to depth of burial.

1.2   CONCLUSIONS

The finite difference calculations of the early ground motion for the JOHNIE BOY event indicated that the best small-scale simulation with PETN would be a sphere with a depth of burial of 0.348 cm of a 1.2 gm charge conducted at 345 g. The results of this simulation were low on crater volume by 22% and high on aspect ratio by 20%. This variation is consistent with the uncertainty in the details of the JOHNIE BOY emplacement[16], the material properties at the time of the event, and the possible variation in the detonation characteristics of the PETN charge. Increasing depth of burial by approximately one charge radius led to a crater volume that was high by 16% and slightly reduced the aspect ratio.

The data from the Boeing tests in both materials (Ottawa sand and desert alluvium) confirm the exchangeability of the charge mass and the cube of gravity, one aspect of centrifuge scaling (i.e., a lack of rate-dependent effects), and no significant perturbations in crater shape due to Coriolis accelerations were observed. However, it was found that crater volume in Ottawa sand was proportional to $Y^{0.84}$ rather than to Y. The tests in alluvium indicate that apparently small changes in test bed density and moisture content can lead to substantial variation in crater dimensions. While these changes are large enough to be observed in well-controlled laboratory experiments, they represent the scatter likely to occur in field events. By understanding these variations, the proper bounds can be established above and below "nominal" cratering curves used for targeting and vulnerability analyses.

Based on analysis of crater dimensions from the centrifuge tests, and on comparison with other near-surface bursts, we conclude that several empirical relations can be written expressing systematic variations in crater dimensions. For scaled yields (see Eq. (19), Section 4.2) less than about 10^4 or 10^5 g's^3 kg,

zero height of burst craters in Ottawa sand and in reconstituted alluvium fall on separate curves. For non-cohesive dry material (e.g., Ottawa sand) crater volume V will be within ten percent of

$$V = \frac{(2.66 \times 10^{-4} m^3)}{\rho} g^{-0.477} W^{0.841} \left(\frac{(U^6 \delta)_{TNT}}{(U^6 \delta)_X}\right)^{-0.159} \quad (1)$$

where ρ is the density in kg/m^3, g is the acceleration in g's (9.8 m/sec^2), W is the charge mass in kg, and U and δ are the Chapman-Jouget (C-J) particle velocity and density, respectively, with the subscripts indicating C-J properties for TNT and the explosive used. For moderately cohesive soils (e.g., reconstituted KAFB alluvium and natural soils for many high explosive field tests) crater volumes obey

$$V = \frac{(6.2 \pm 2.2) \times 10^{-5} m^3}{\rho} g^{-0.070} W^{0.977} \left(\frac{(U^6 \delta)_{TNT}}{(U^6 \delta)_X}\right)^{-0.023} \quad (2)$$

There are no data for high explosive craters in alluvium at scaled yields higher than about 10^5 g's^3 kg, but it is expected that they would have volumes closer to (1) than to (2). Craters at non-zero heights of burst will have volumes given by (1) or (2) multiplied by $10^{-0.115H/W^{0.279}}$ where H is the height of burst in m. If the same $W^{0.28}$ height of burst scaling is applied to nuclear craters, it is found that crater volumes from 1kt nuclear bursts in alluvium and all of the Pacific nuclear craters fit a single height of burst and yield relation

$$V = V_0 Y^{0.84} 10^{-0.49H/Y^{.28}} \quad (3)$$

where $V_0 = 3.5 \times 10^3 m^3$ per kt$^{0.83}$ for events in alluvium, $V_0 = 1.1 \times 10^4 m^3$ per kt$^{0.83}$ for events in coral sand with a normal device and $V_0 = 7 \times 10^4 m^3$ per kt$^{0.83}$ for tank shots.

Crater aspect ratios were found to be independent of scaled yield and the shape factor $V/\pi R^2 d$ is only weakly dependent on scaled yield (to the 0.041 power). By comparison high yield Pacific nuclear events exhibit a definite yield dependence of aspect ratio. Deviations of individual Pacific crater volumes and aspect ratios from the overall trend of the Pacific data with yield show a strong correlation indicative of either cause and effect or mutual cause.

1.3   RECOMMENDATIONS

The centrifuge tests which have been performed so far indicate the importance of attention to detail in test bed preparation. If care is not used, scatter in the laboratory will be as large as in field events, and important features of the data may be obscured. The tests conducted by Schmidt have shown both that careful preparation can lead to excellent reproducibility and that seemingly minor variations in test bed assembly can lead to significant changes in the results.

We suggest that the next series of tests be conducted in saturated coral sand in an effort to reproduce the results of the PACE series of relatively small (1000 lbs. of TNT) high explosive events. If the simulation of these events proves successful, an attempt to reproduce the CACTUS results on a small scale might be undertaken next. This would require the development of a high explosive equivalence for this event.

The centrifuge facilities currently available are too small to achieve a direct simulation of a megaton nuclear surface burst. In order to understand the large aspect ratios observed on the events at the PPG with yields above 40 kT, it will be necessary to hypothesize a physical mechanism to be tested on the centrifuge with a test bed material modified to enhance the proposed effect at smaller scale. The possibility of liquifaction-enhanced slumping is one example of a mechanism which could be explored through selected variation in test bed properties.

Once the general trend of the high yield data is understood, one could proceed to a detailed study of each source, emplacement and geologic media in

9

an attempt to differentiate the scatter from the general trend for individual events. We suggest that a return to geologic media of strategic interest be given higher priority at this stage of program evolution.

2. GEOTECHNICAL TESTING BY CENTRIFUGE

2.1 BACKGROUND

The use of a centrifuge to test the response of model soil and rock structures was initiated at about the same time in the early 1930's in both the United States by P. B. Bucky,[17] and in the Soviet Union by G. I. Pokrovsky.[18-20] Bucky performed tests on the stability of mine openings by using very small models in a centrifuge having an arm radius of about 0.2 meters. The tests were conducted at centrifugal accelerations up to 2,000 g's. Bucky postulated that his techniques could be extended to accelerations of up to 15,000 g's on an apparatus with an arm radius of 3 meters. Apparently, the technique did not meet with wide acceptance in geotechnical work in the United States, and only a few subsequent experiments have been carried out.

In contrast, the work begun by Pokrovsky and his colleague I. S. Fyodorov in the USSR led to widespread use of centrifuges for soil engineering purposes in the Soviet Union.[21]* The USSR effort has also considered explosive phenomena. They have conducted simulations of explosive loading of underground structures and simulations of HE cratering for both surface bursts and shallow depths of burial.[10,21]

In the early 1960's, H. Ramberg, a Swedish geologist and a number of his students began an extensive series of tests of model geological structures, in studies of the stability of various tectonic processes.[22,23] In the middle 1960's, A. N. Schofield in England investigated the stability of clay slopes under rapid drawdown conditions.[24-26] He constructed a large centrifuge having an arm radius of 1.5 meters, and capable of carrying a 750 kg package to an acceleration of 130 g's. This machine was constructed at the University of Manchester Institute of Science and Technology (UMIST). An even larger centrifuge was constructed at the University of Manchester under the supervision of P. W. Rowe.[27] Experience has now been accumulated from a large number of model tests of soil structures carried out on these centrifuges. At Cambridge University, where Schofield began his centrifuge studies, work by K. H. Roscoe and C. P. Wroth,[28]

---

*Although the publication date of this book is 1969, its English translation has only recently become available through the efforts of A. N. Schofield.

continued on the centrifuge facility rented from a British aerospace company while design and construction proceeded on a much larger facility (5 meters radius, acceleration to 300 g's). This centrifuge has been completed and preliminary studies are now under way.

Geotechnical work has also been done on centrifuges in Japan, Denmark, France and South Africa.[29-33] A literature review of centrifuge testing in soils is given in Reference 34.

In 1975, a symposium on the use of centrifuges in modeling geotechnical phenomena was organized at the California Institute of Technology by R. F. Scott. Representatives from the U. K., Sweden, Canada, and many U. S. universities gathered and presented their research using this technique. Representatives of the Ames Aeronautical Laboratory proposed refurbishing their centrifuge for this purpose. This would provide a facility to accelerate payloads up to approximately five metric tons to as much as 200 g's. The arm radius is 17 m and the workspace would be 10.6 m^3.

Sandia Laboratories is currently operating two centrifuges, with a 7.6 and 10.7 meter radius arm. The arm has a design strength of 7.3 x 10^5g-kg to 200 g's. Larger g's are possible. The working section is enclosed, and provides a space of about 7.1 m^3.

In the USSR, the cratering due to buried charges has been investigated for sands and clays having various moisture content.[21] In particular, an experiment was conducted at the VODGEO Institute which utilized a plastic clay with the moisture content of 18%. A g enhancement of 100 was used. The Russians claim agreement between the model crater and the prototype crater volume to 5.8%. Tests have also been conducted in clayey loam. By emplacing thin layers of sand in these media, the Soviet researchers have been able to measure the deformation of the medium near the crater.

2.2   THEORY

In this section it will be shown that small model HE tests in a centrifuge simulate large-scale HE events at normal gravity. Gravity plays a more important

12

role in the large-scale event, and the enhanced g's in the small experiment simulate this effect. If the experiment is properly designed, many important material properties scale exactly, provided that the model is made of the same material as the prototype. Thus, it is not necessary to seek or develop new materials to use in the model.

It is shown that if the dimensions of the model are reduced by the same factor as the g enhancement, then the usual "hydrodynamic" scaling laws are obeyed. This scaling leaves the units of velocity, specific internal energy, density, and pressure invariant. As a result, material moduli and their dependence on specific internal energy (or temperature) are preserved. Plastic effects of a very general nature are preserved, including those described by the most complex cap models. As is usual in hydrodynamic scaling, rate effects or effects having an inherent characteristic length, do not scale. However, failure or fracture processes which are described in terms of strains and/or stresses, will scale correctly.

The equation-of-state of high explosives and air scale properly. Thus, the same high explosives could be used in the model as in the prototype. If difficulties are encountered with attaining detonation in small models of the HE used in the prototype, then an alternate HE having a similar Chapman-Jouget pressure and thermodynamically similar explosive products can be used. Since the EOS of air scales properly, the effects of air blast and overpressure will be correctly modeled.

2.2.1 Hydrodynamic Scaling

It will be assumed that readers of this report are familiar with the usual "hydro" type of scaling. In "hydro" scaling the physical parameters of density, ρ_0, modulus, μ_0, and a characteristic length, D, are prescribed. We adopt the point of view that ρ_0 and μ_0 are constant,[*] but D is permitted to vary. For example, it can be the characterisic dimension of one of a set of geometrically similar configurations. As shown in Table 1, a characteristic velocity is prescribed by the sound speed, $c^2 = \mu_0/\rho_0$ so that a unit of time = D/c can be constructed. This implies that as the unit of length is increased, the unit of time is increased

_____

[*]The equation-of-state can be a non-linear function of density and specific internal energy in which the parameters ρ_0 and μ_0 appear.

13

Table 1
Comparison of Scalings

QUANTITY	DIMENSIONS	"HYDRO" ρ, μ, D $c^2 = \mu/\rho$	FROUDE ρ, g, D	CENTRIFUGE $gD = U^2 = const$
Length	L	D	D	D
Mass	M	ρD^3	ρD^3	ρD^3
Time	T	D/c	$\sqrt{D/g}$	D/U
Velocity	L/T	$c = \sqrt{\mu/\rho}$	$\sqrt{gD}$	U
Pressure	M/LT^2	ρc^2	ρgD	ρU^2
Specific Internal Energy	L^2/T^2	c^2	gD	U^2
Energy	ML^2/T^2	$\rho c^2 D^3$	ρgD^4	$\rho U^2 D^3$
Kinematic Viscosity	L^2/T	cD	$D\sqrt{gD}$	UD

14

by the same factor. As Table 1 shows, the units of velocity, pressure, and specific internal energy remain invariant under this type of size scaling. The constitutive relations remain invariant also if they are couched only in terms of strain, stress, and specific internal energy. Nonlinear or hysteretic models still scale appropriately as long as they are couched in terms of the above variables. This includes complex void crushing models, such as the P-α model of Herrmann.[35] It also includes plastic models, such as the von Mises, Mohr-Coulomb, or Prager-Drucker, and plastic–dilatant models as prescribed by the cap. It is seen that the energy behaves as D^3, which implies that D is proportional to $W^{1/3}$, which is the genesis of the widely used term "$W^{1/3}$ scaling".

The unit of kinematic viscosity is equal to cD. This means that when the differential equations describing the motion are rendered dimensionless by this set of units, the dimensionless kinematic viscosity will be larger for smaller scale models. Thus, the effects of viscosity are enhanced in smaller events. Viscosity is just one manifestation of a strain rate effect, and one can deduce that in general strain rate effects are enhanced at smaller sizes.

2.2.2 Froude (Gravity) Scaling

If one considers the effects of gravity, he has at his disposal the physical units of ρ, g, and D. The units generated from these quantities are shown under the heading Froude in Table 1. As the table shows, the unit of pressure is given by gD. The dependence of the unit of pressure on D destroys dynamic similitude. That is, if one considers a smaller model, the dimensionless moduli which appear in the constitutive relations will be larger than in the large prototype. This implies that in a constant gravity field, a large-scale experiment will behave as though the moduli were weaker than in a small-scale one. Similarly, the unit of specific internal energy is gD. The internal energy released per gram is an important parameter for high explosives, and the dependence of this unit on D provides a serious perturbation to scaling high explosive phenomena. It is seen that the energy in this scaling depends on D^4, so that when this type of scaling is appropriate, lengths vary as $W^{1/4}$, and times as $W^{1/8}$.

2.2.3 Centrifuge Scaling

The key point of this section is that the enhanced effects of gravity in

larger events can be taken into account, and dynamic similitude preserved, if one scales the unit of length down by the same factor that the unit of gravity is scaled up. This will be termed centrifuge scaling. In this scaling, the product gD is a constant which we term U^2. U has the dimensions of velocity, and it is seen from the last column in Table 1 that it plays the same role in determining units as c does in hydro scaling. The basic assumption in centrifuge scaling is that rate effects are not important.

As a specific example, suppose one wished to simulate a 500 metric ton HE sphere detonated half-buried in a soil medium. If the experiment were modeled in a centrifuge at 500 g's, each linear dimension in the model would be reduced by a factor of 500. The HE sphere radius, assuming a loading density of 1.5 g/cm^3, would be 4.30 m in the prototype and 0.86 cm in the model. The experiment would start with the small sphere half-buried in the same soil as the prototype, and with air above it. When the model charge is detonated at its center, the explosive detonation wave propagates at the same speed as it would in the prototype, and generates the same pressure. Since the model is 500 times smaller than the prototype, the wave reaches homologous* points in the model at times 1/500th of those in the prototype. In particular, it reaches the sphere's surface in 1/500th of the time. When the shock propagates into the ground and air, it generates shocks having the same pressures as in the prototype, and having the same velocities. This is true even if the model is soil having extreme non-linearity and hysterisis. The shock propagating into the air is similarly modeled.

Again, the shocks attain homologous points in 1/500th of the time in the model because of its smaller size. The pressure and velocity profiles behind the shocks should be scale models of each other at corresponding (scaled) times. The gravitational effects are the same in the model and prototype because the 500-fold gravity in the model acts for 1/500th of the time. Thus, the ejecta trajectories in the model should appear exactly as those in the prototype if slow motion photography of the model slowed them down a factor of 500. Other ground motions, occasioned by both the direct shock and by the air overpressure, should also be scale models of each other in both time and space. When the event is

*Homologous points are corresponding points in the model and prototype.

16

over, the crater and ejecta* in the model should be scale models of the real event.

2.3 MINIMIZING THE CORIOLIS EFFECT

The Coriolis acceleration $\vec{a}_c$ in a rotating system is given by

$$\vec{a}_c = -2\vec{\omega} \times \vec{v} \tag{5}$$

where $\vec{\omega}$ is the angular velocity of the rotating system, and $\vec{v}$ is the velocity with respect to the rotating system. The acceleration is produced with respect to the rotating coordinate system by the tendency of particles to move in a straight line in fixed space. Because the measurements in a centrifuge will be taken with respect to the rotating system, it will provide perturbations to the experiment.

The magnitude of the Coriolis acceleration is

$$\vec{a}_c = 2\omega v \sin \gamma \tag{4}$$

where γ is the angle between the angular acceleration and velocity vectors. The Coriolis acceleration is therefore largest when the velocity is normal to the centrifuge's axis of revolution ($\gamma = 90°$). It is zero when the velocity is parallel to the axis ($\gamma = 0°$). Thus, there are two directions in the environment in which the Coriolis acceleration is zero.

A measure of the perturbation is given by the relative magnitude of the Coriolis acceleration and that of the centrifuge, which we call g. Therefore, the perturbation is given by

$$a_c/g = \frac{2\omega v \sin \gamma}{\omega^2 r} = \frac{2v \sin \gamma}{\sqrt{gr}} \tag{6}$$

We can see from this equation that a_c/g is smallest when g and r are

*This is true if Coriolis accelerations can be neglected compared to the centrifugal acceleration. To minimize Coriolis accelerations, one should use as long a centrifuge arm, and work at the highest g's possible. This is discussed in the next section.

largest. (We recall from the discussion on scaling that the velocity is invariant at homologous points in the model and prototype.) Therefore, it is desirable to work at the largest value of g and r possible to minimize effects due to the Coriolis acceleration. If we work at a given g level, the Coriolis effect is minimized by using the largest radius arm possible.

Lack of symmetry in the final crater shape provides an indication when Coriolis effects have been important. No such effect was observed in the Boeing tests discussed in Section 4.

3. HIGH EXPLOSIVE CHARGE EQUIVALENCE FOR JOHNIE BOY

A major portion of our program was devoted to determination of the spherical PETN charge which best simulates the JOHNIE BOY event. The JOHNIE BOY source had a yield[36] of 0.5 ± 0.2 kT and a depth of burial of 0.585 m. This event was conducted at Area 18 of the Nevada Test Site (NTS). The resulting apparent and true crater profiles are shown[36] in Figure 1. These profiles are in good agreement with the apparent crater dimensions of 18.6 m, 9.33 m and 4,113 m^3 for radius, depth and volume given by Vortman.[12]

Several criteria led to the choice of JOHNIE BOY for detailed study. First, we were looking for an event at a dry, homogeneous site. Second, the yield of the event and size of the final crater should be on a scale that could be simulated at the Boeing facility. Third, of the various nuclear cratering events at NTS, JOHNIE BOY had been the most extensively studied.

The main uncertainties in using JOHNIE BOY as a standard to validate centrifuge scaling should be recognized at the outset of this discussion. Some of these points will be brought out in more detail in the following sections. First, the details of source emplacement were not clearly documented at the time of the event. Sensitivity studies have not been performed to explore what variations in energy coupling are plausible. The alluvium properties of Area 18 are poorly known. Data from other sites were used to construct the material response model. While PETN may be considered as well characterized as any explosive, its detonation properties are quite sensitive to small amounts of air voids. The precise packing density of the charges used in the Boeing tests was not known at the time the calculations discussed here were performed, but calorimeter tests[15] on similar charges suggested that a variation of $\pm 20\%$ in detonation energy might be expected. Although this list of uncertainties may appear formidable, we felt that a simulation which reproduced apparent crater volume to within 30% and linear dimensions to 10% was an ambitious, but not impossible goal. Results were 22% in volume, 16% in depth and virtual agreement in radius.

In Section 3.1, we present the criteria used to establish charge equivalence. Material models are summarized in Section 3.2. Results of the final

19

calculation are given in Section 3.3. Sensitivity studies are summarized in Section 3.4. The results of the centrifuge tests are discussed in Section 3.5.

3.1   EQUIVALENCE CRITERIA

The calculations described in Reference 36 were chosen as the standard for determination of charge equivalence. Thus, we introduce the additional uncertainty of the effect of different codes used by different groups at different times. Comparisons of codes in the past using identical starting conditions have led to variations in the final results as large as any of the uncertainties mentioned in the previous section.

The energy partition in the ground beyond a range of 3.6 meters is shown in Figure 2. One can see that the energy coupling is essentially complete after several miliseconds. It is on this time scale that we presume the details of the source become unimportant and the nuclear to high explosive equivalence can be established. As in previous studies[37] for buried cratering sources, attention is initially focused on the kinetic energy in the flow.

Maxwell[38] noted from a study of several surface-burst calculations that the cratering flow had features consistent with steady-state flow of an incompressible fluid in the region behind the shock wave after the stresses had relaxed to low values. In order to achieve a quantitative measure of this observation, concentric surfaces $S_i(0)$ ($i = 1,2,...$) were prescribed at $t = 0$ as illustrated in Figure 3a. Each surface was defined by Lagrange grid points in the computational mesh that moved with the flow as illustrated in Figure 3b. The volume $V_i(t)$ enclosed by the surface $S_i(t)$ and the original ground plane and its time rate of change $\dot{V}_i(t)$ were observed to obey the relationship

$$\dot{V}_i(t) = \beta / V_i^{\alpha}(t) \tag{7}$$

where α and β were independent of time and index i after the shock had passed and the stresses had relaxed. If one defines the mean radius

$$\bar{R} = (3V/2\pi)^{1/3}, \tag{8}$$

20
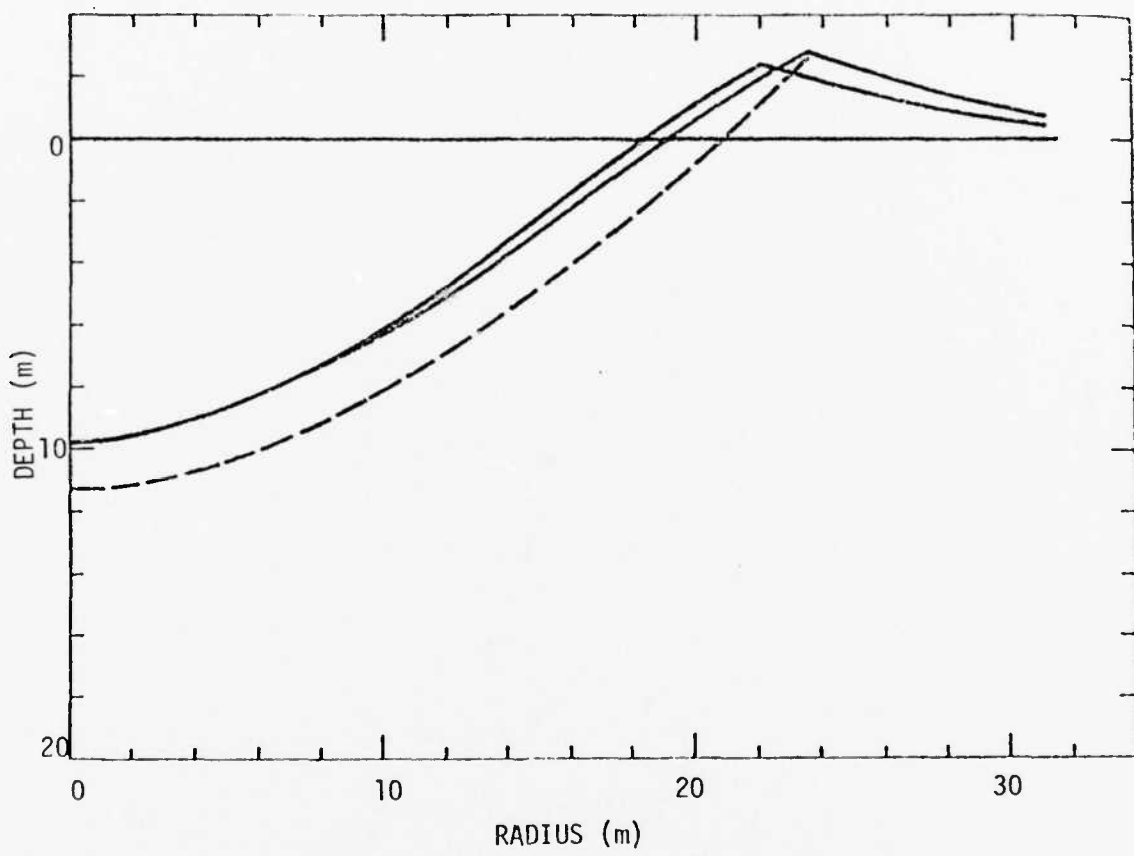
Figure 1. Two sections of JOHNIE BOY apparent crater (solid lines) and true crater (dashed lines).
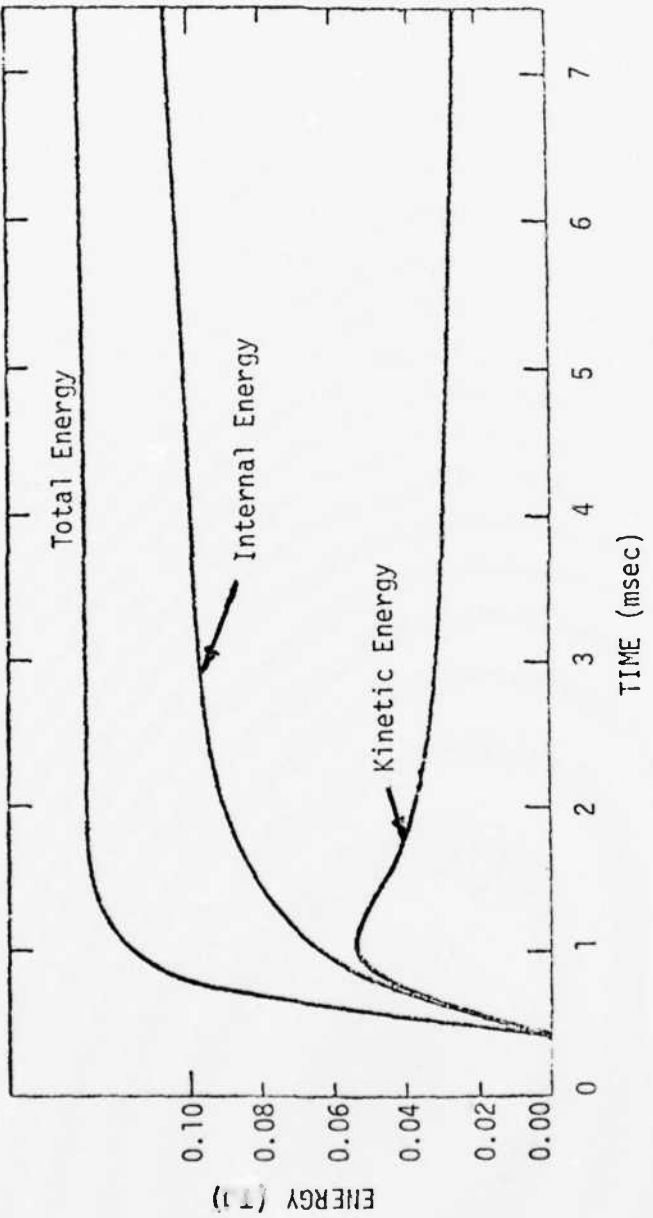
Figure 2. Partition of energy versus time in the ground beyond the range of 3.6 meters.

22

Original ground surface

$S_1 (0)$
$S_2 (0)$
$S_3 (0)$ ...
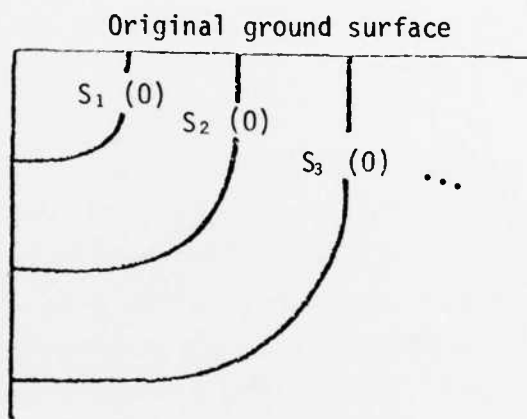
Figure 3a.   Schematic concentric reference surfaces at t=0.

$V_i(0)$ $S_i(0)$

$V_i(t)$ $S_i(t)$
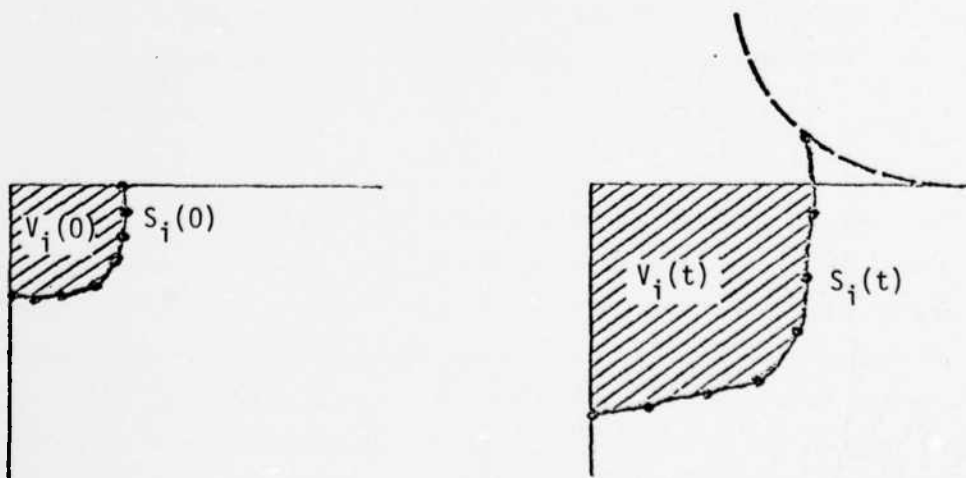
Figure 3b.   Reference surface S_i and its associated volume V_i at t=0 and t>0.

and mean radial velocity

$$\dot{\bar{R}} = \dot{V}/2\pi\bar{R}^2,$$ (9)

the equivalent observation is

$$\dot{\bar{R}} = \alpha/\bar{R}^Z .$$ (10)

One can think of α as a measure of the kinetic energy of the flow and Z as a measure of the geometry of the streamlines. For purely radial flow, Z = 2.0. These general observations form the basis for the hypothesis that a complex, high energy source might be simulated by variation in the yield and depth of burial of a spherical high explosive charge. Although the parameters are cross-coupled, it was expected that α would depend strongly on charge yield and Z would depend most strongly on depth of burial.

Application of this analysis[38] to the JOHNIE BOY calculation led to the results shown in Figures 4 and 5. One can see that the results are quite consistant with Eq. (10) for the values Z = 2.71 and α = 2.44 x 10^4 in mks units. Some deviation is apparent at times beyond 100 msec when gravity and strength effects cause a breakdown of the steady-state assumption. The most severe test of Eq. (10) is illustrated in Figure 6, where the space-time motion of the surface which started at 3.6 m is compared with the model.

3.2 MATERIAL PROPERTIES

3.2.1 Alluvium

The material properties at the JOHNIE BOY site (Area 18 at NTS) are poorly known. Data from other sites were used to establish the model for the previous calculations of this event. We have used this same data base to choose parameters in our model for the response of geologic materials. The initial density, bulk modulus and shear modulus were given the values of 1.8 g/cm^3, 7.717 kbar and 5.5 kbar used in the earlier models. The load and unload curves which form the envelope of the irreversible compaction region are shown in Figure 7. An air-void content of 19% is presumed.

The EOS of the void-free material has been given previously by Allen.[39]

24
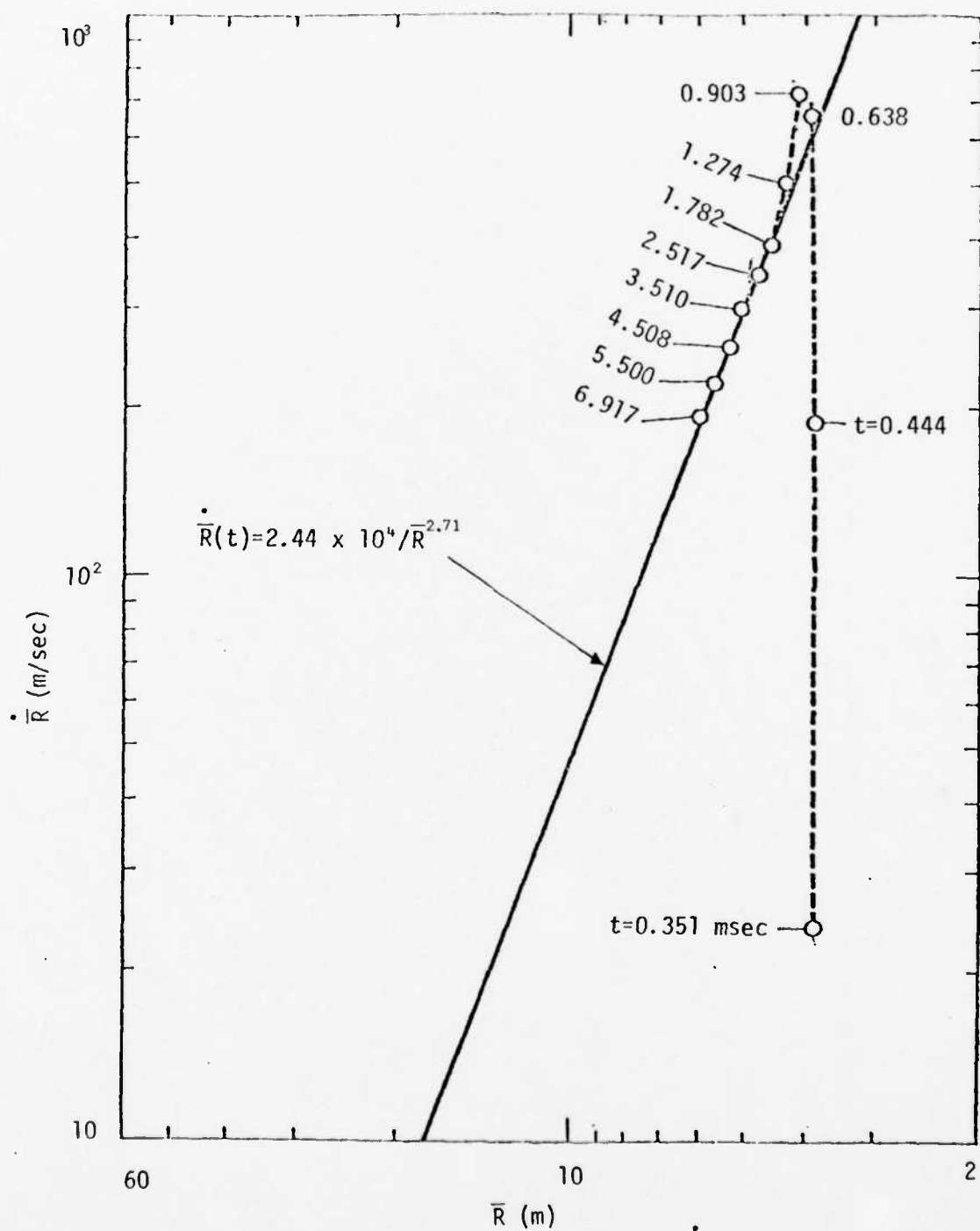
Figure 4. Innermost reference surface $\bar{R}, \dot{\bar{R}}$ points at various times.
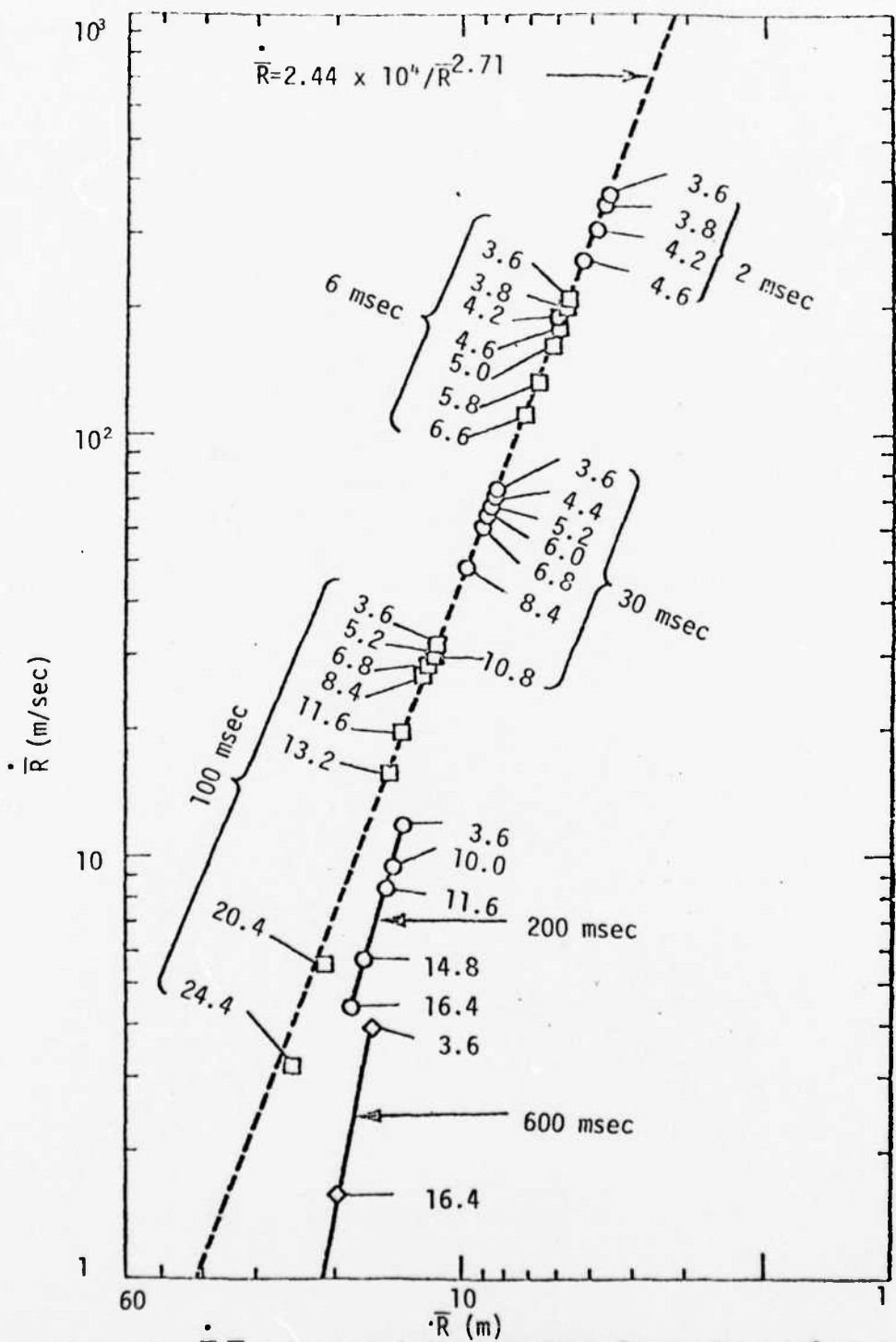
Figure 5. $\dot{\overline{R}}, \overline{R}$ points at indicated times for various reference surfaces with indicated initial radii (meters).

26
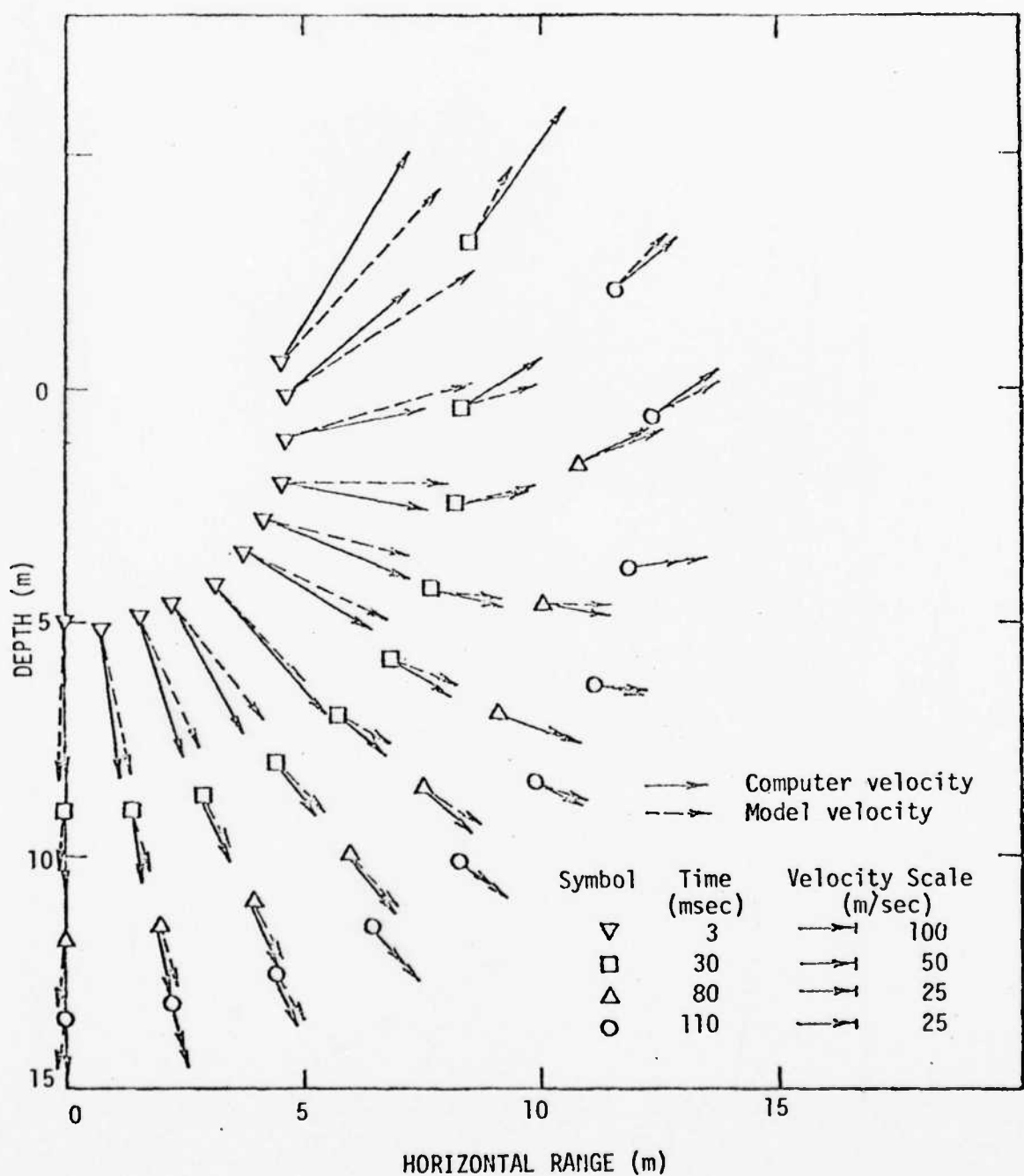
Figure 6. Model velocities (dashed arrows) compared to computed velocities (solid arrows) at selected points and times.

27
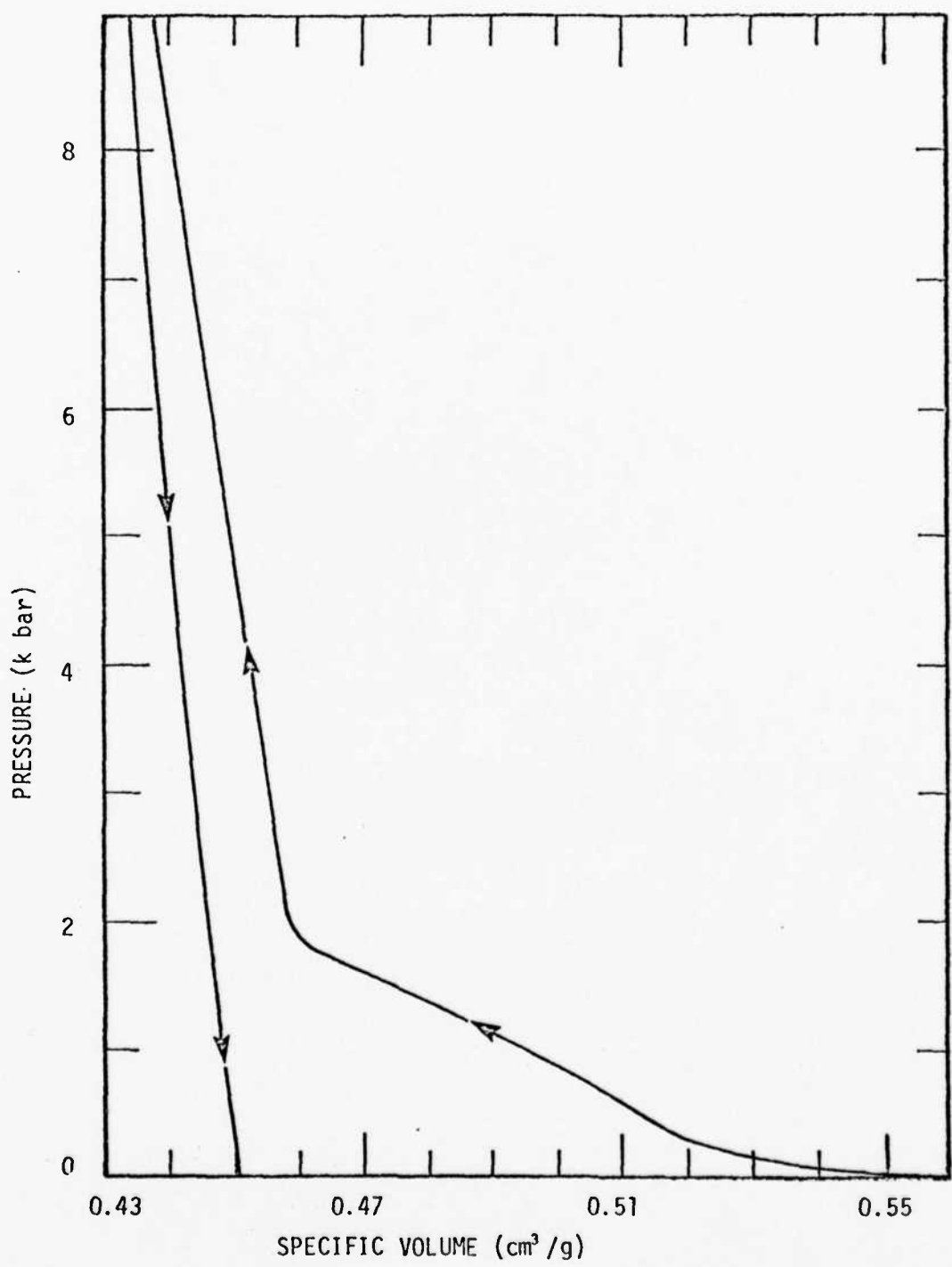
Figure 7. Alluvium crush curve.

28

For condensed states $(\rho/\rho_0 > 1)$ and for any cold states $(\varepsilon < \varepsilon_s)$

$$P = P_C = A\mu + B\mu^2 + \Gamma\rho\varepsilon \tag{11}$$

where $\mu = \eta - 1$, $\eta = \rho/\rho_0 = v_0/v$

$$\Gamma = a + \frac{b}{\dfrac{\varepsilon}{\varepsilon_0 \eta^2} + 1} \tag{12}$$

For expanded hot states $(\rho/\rho_0 < 1$ and $\varepsilon > \varepsilon_s')$

$$P = P_e = a\varepsilon\rho + \left[\frac{b\varepsilon\rho}{\dfrac{\varepsilon}{\varepsilon_0 \eta^2} + 1} + A\mu e^{-\beta(v/v_0 - 1)} \right] e^{-\alpha(v/v_0 - 1)^2} \tag{13}$$

A smooth transition between the condensed and expanded states is insured by a transition equation for the intermediate region defined by $\varepsilon_s < \varepsilon < \varepsilon_s'$ and $\rho/\rho_0 < 1$. This blended portion of the equation of state has the form:

$$P = \frac{(\varepsilon - \varepsilon_s) P_e + (\varepsilon_s' - \varepsilon) P_C}{\varepsilon_s' - \varepsilon_s} \tag{14}$$

In these equations, ε, ρ and P are density, specific internal energy, and pressure. The values of the constants used for JOHNIE BOY alluvium are given in Table 2.

A non-associative flow rule was used with the yield surface shown in Figure 8. At the early times of flow development studied here, the details of the treatment of the strength of the alluvium are unimportant.

3.2.2 PETN

The Jones-Wilkins-Lee (JWL) equation of state [40] for detonation products of explosives can be written in the form:

$$P = A\left(1 - \frac{\omega}{R_1 v}\right)e^{-R_1 v} + B\left(1 - \frac{\omega}{R_2 v}\right)e^{-R_2 v} + \omega\rho\varepsilon . \tag{15}$$

29

Table 2

Parameters for JOHNIE BOY Alluvium

Parameter	Value	Units
A	2.34×10^{11}	dynes/cm^2
B	1.02×10^{11}	dynes/cm^2
a	0.5	-
b	1.3	-
ρ_0	2.22	g/cm^3
ε_s	3.5×10^{10}	ergs/g
ε_s'	1.8×10^{11}	ergs/g
ε_0	2.01×10^8	ergs/g
α	5.0	-
β	5.0	-
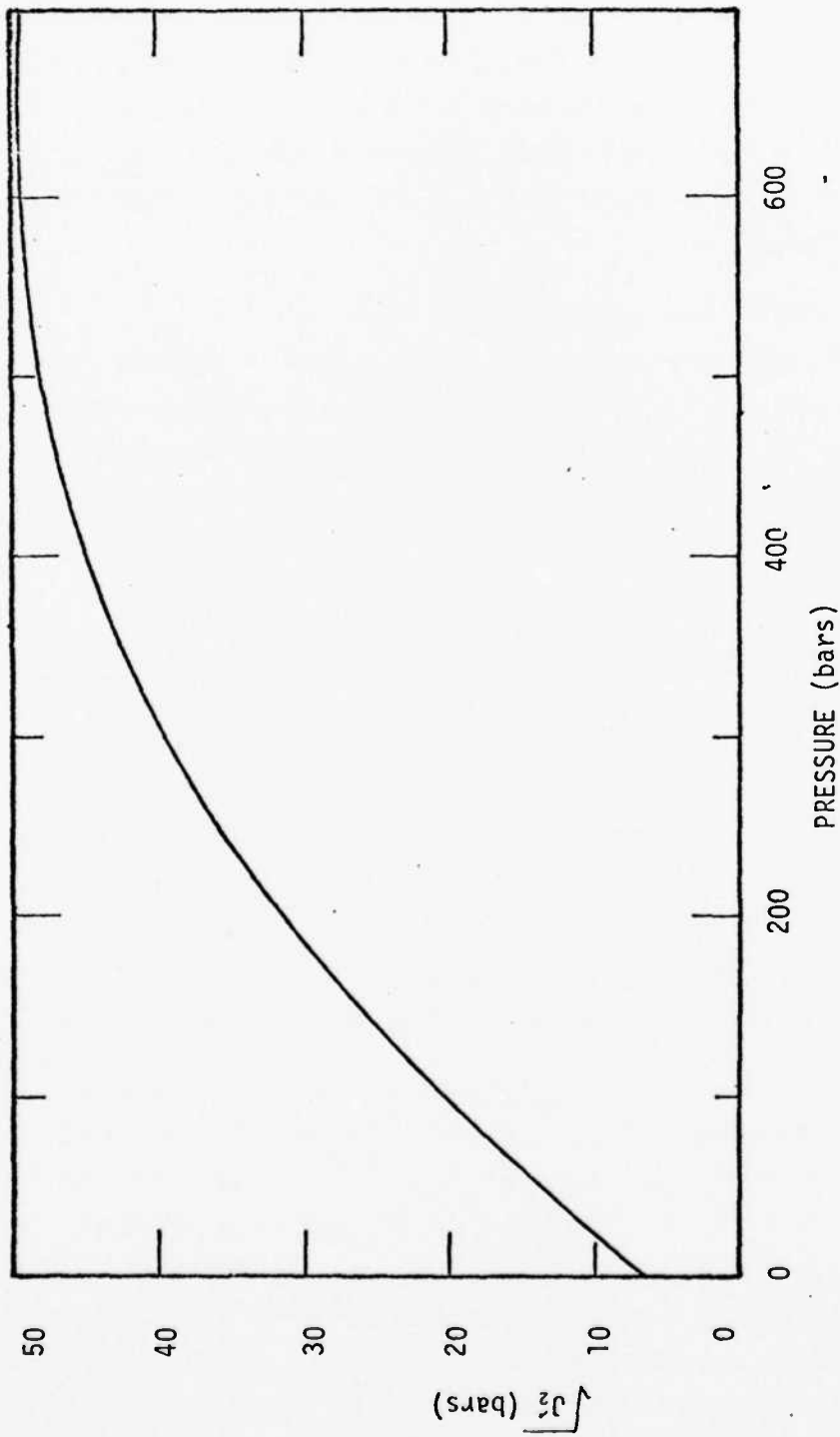
Figure 8. Alluvium yield surface.

where ε is the specific internal energy, ρ is density and $v = \rho_0/\rho$. The values of the various parameters for PETN (with $\rho_0 = 1.77$ g/cm^3) are given in Table 3 along with the heat of detonation ε_0 and detonation velocity D. As was mentioned earlier in this section, the detonation properties of PETN are sensitive to packing density. This variability is illustrated in Figure 9 from Reference 15. Calorimeter tests indicated a variability of up to 20% in heat of detonation for charges similar to those used in the Boeing tests.

3.3   RESULTS OF FINAL SIMULATION PREDICTION

A number of charge sizes and depths of burial were investigated before our final choice was made. The results of these preliminary calculations are briefly summarized in Section 3.4. Our last calculation incorporated a charge with an initial radius of 1.88 m and a depth of burial of 1.20 m. This charge has a total mass of 4.93×10^4 kg and a total yield of 2.81×10^{11} J. Thus, the high explosive to nuclear energy equivalence factor represented by this charge is 0.134.

The initial grid configuration is shown in Figure 10. An expanded plot of the zoning in the high explosive sphere and its immediate surroundings is given in Figure 11. The first 0.2 msec of the calculation, which is the time for the spherical HE burn, was performed with a one-dimensional code so that the development of the detonation wave could be provided adequate resolution. Profiles of pressure and particle velocity at the time of overlay into the two-dimensional grid are shown in Figures 12 and 13. The final grid configuration in the ground and lower portion of the high explosive is shown in Figure 14 while the interfaces in the upper region of interaction with the air are illustrated in Figure 15.

As can be seen in Figure 11, a hemi-spherical surface in the ground at a radius of 3.6 m was established in the initial grid generation and maintained for editing purposes and comparison with the equivalence criteria outlined in Section 3.1. The kinetic energy in ground material beyond this surface is compared with the JOHNIE BOY results in Figure 16. The motion of the reference surface, averaged as discussed in Section 3.1, is compared with the JOHNIE BOY results in Figure 17. We consider this comparison to be very favorable. Finally, the detailed velocity fields of the reference surface are compared in Figure 18. Again the

32

Table 3

EOS Parameters for PETN

Parameter	Value	Units
ρ_0	1.77	g/cm^3
R_1	4.4	-
R_2	1.2	-
A	6.17×10^{12}	$dynes/cm^2$
B	1.69×10^{11}	$dynes/cm^2$
ω	0.25	-
ε_0	5.7×10^{10}	ergs/g
D	8.3×10^3	m/s
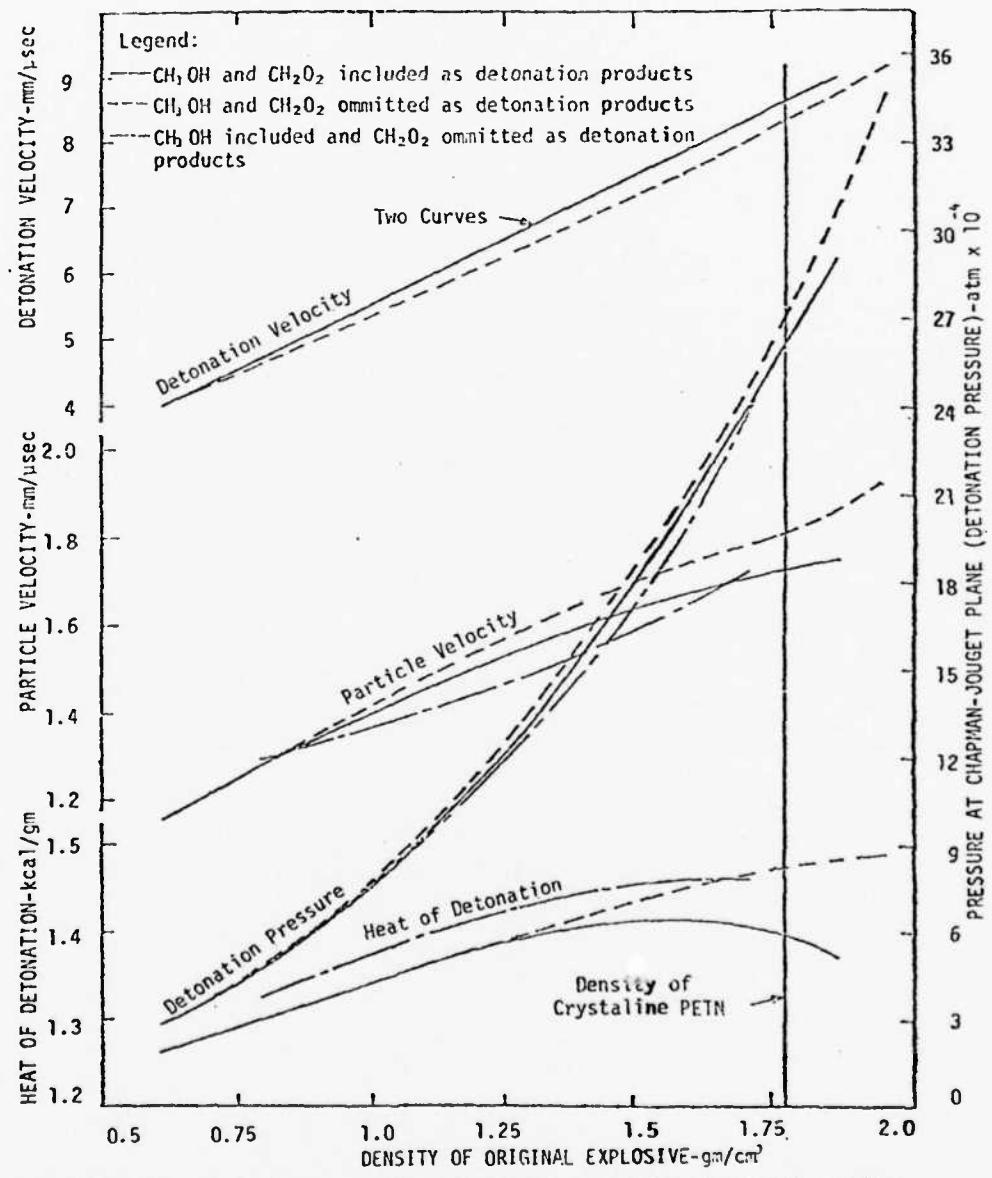
Figure 9. Explosive properties of PETN as a function of initial density.
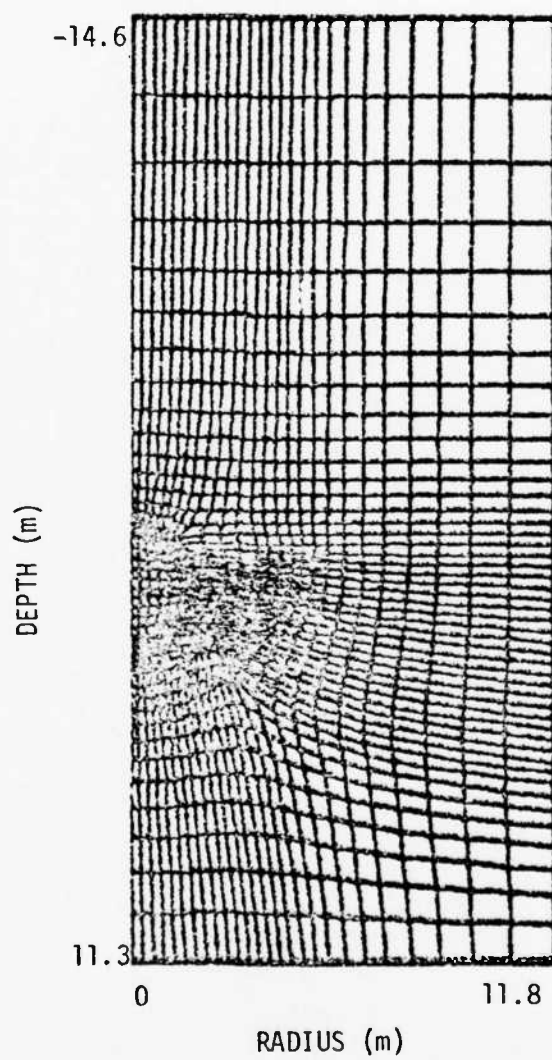
Figure 10.   Initial grid for final simulation
             prediction.
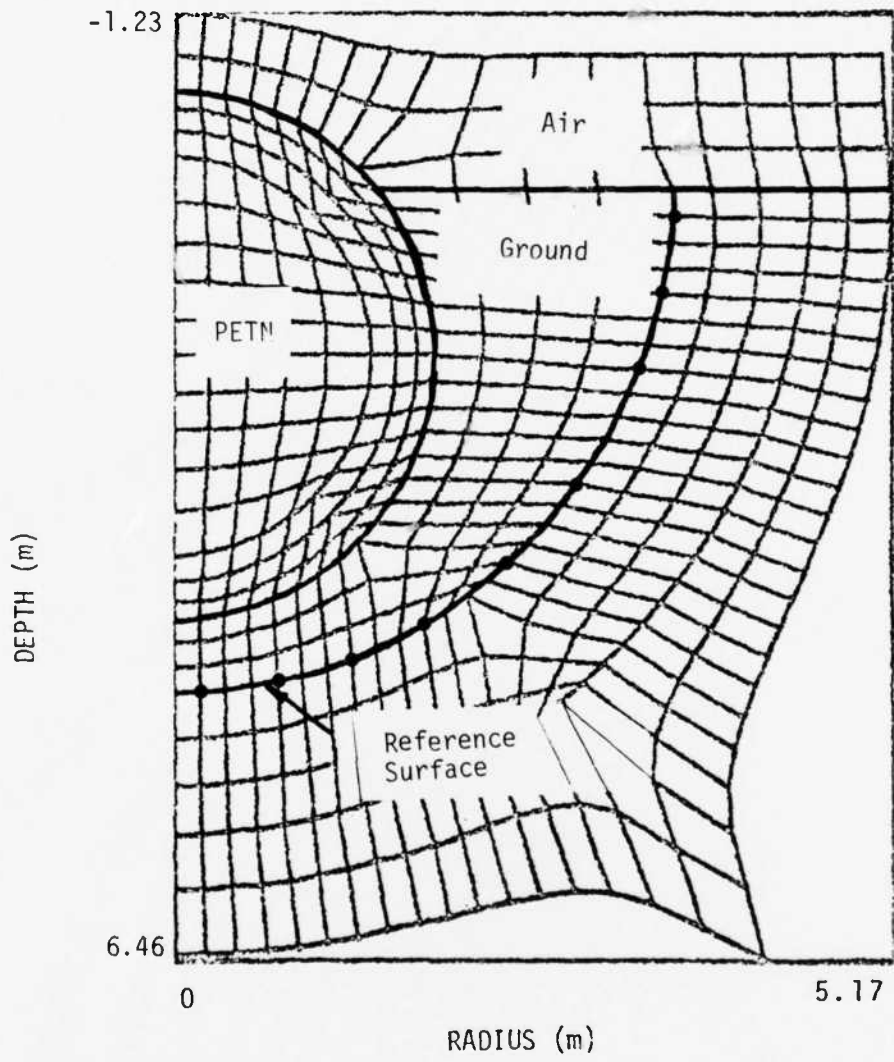
Figure 11. Grid detail near PETN sphere.
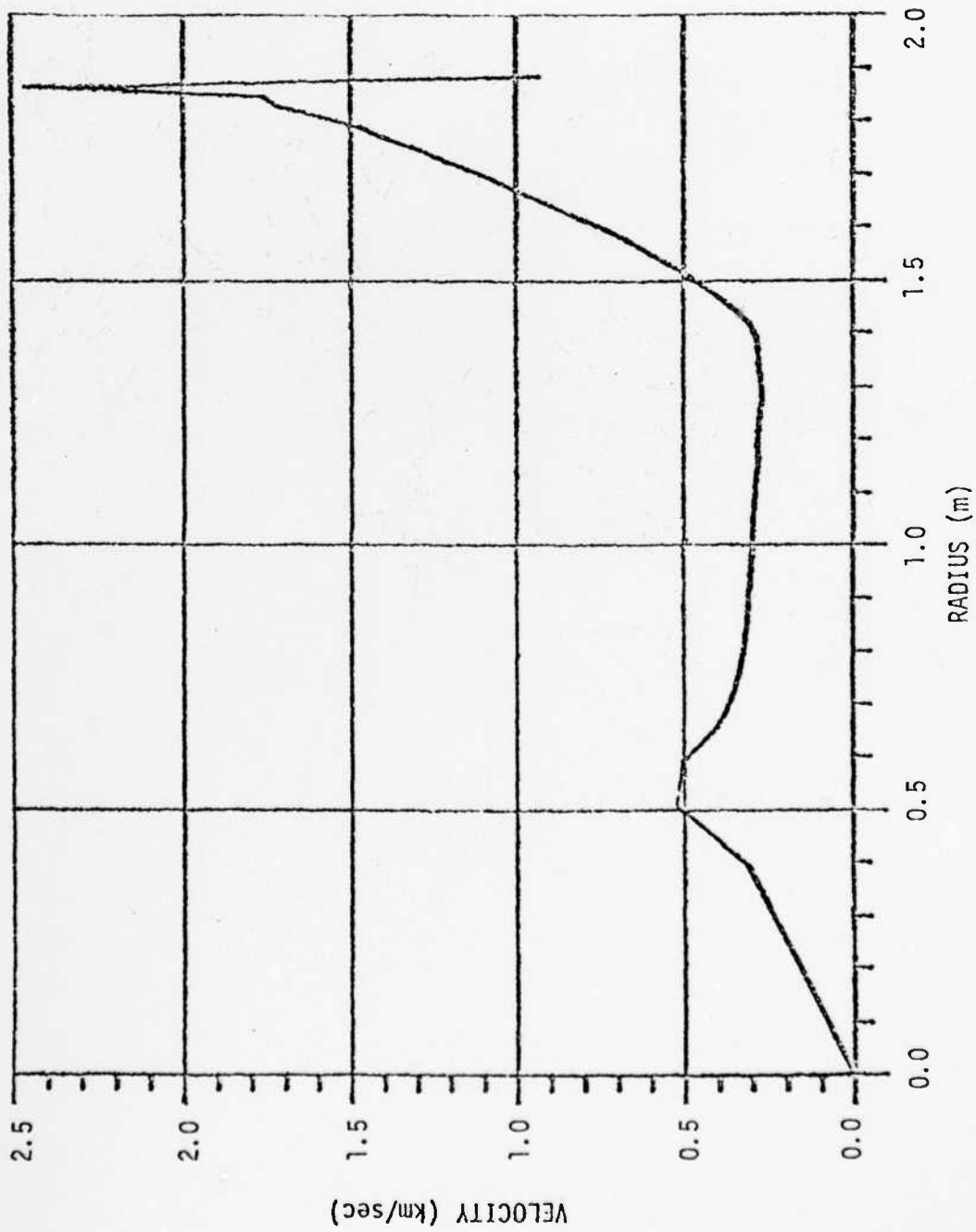
Figure 12. Particle velocity distribution in PETN at termination of burn.
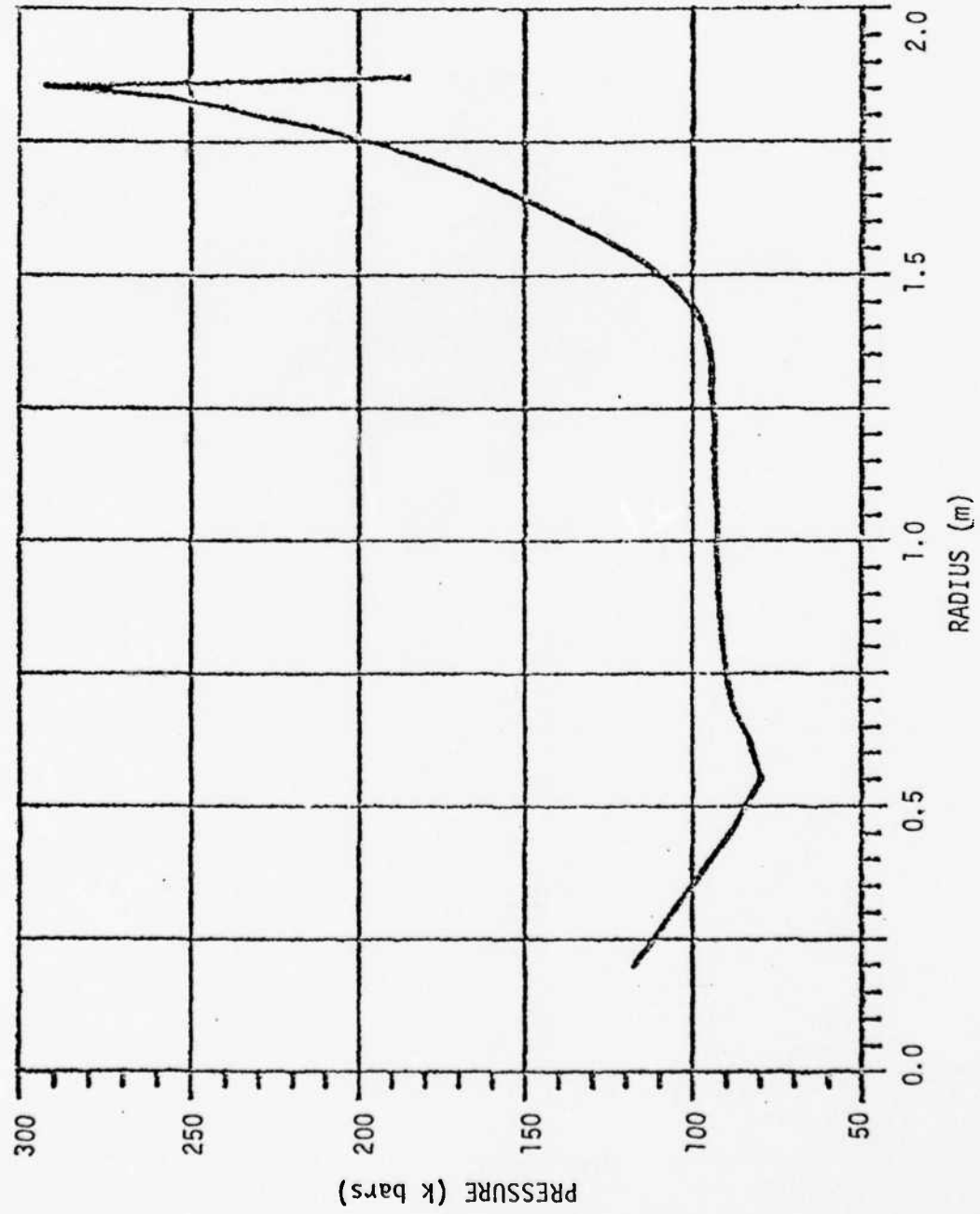
Figure 13. Pressure distribution in PETN at termination of burn.

38
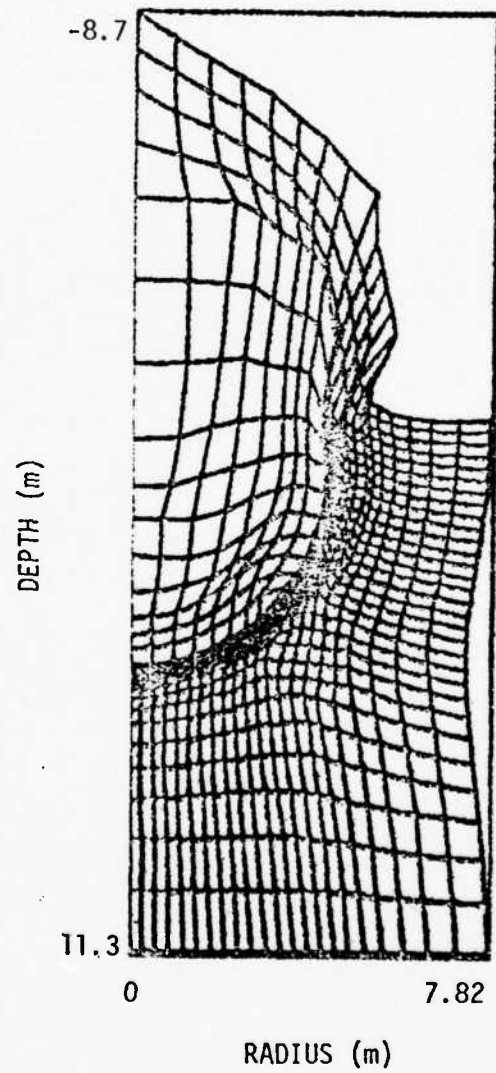
Figure 14.   Final grid configuration near bottom half
             of the source.
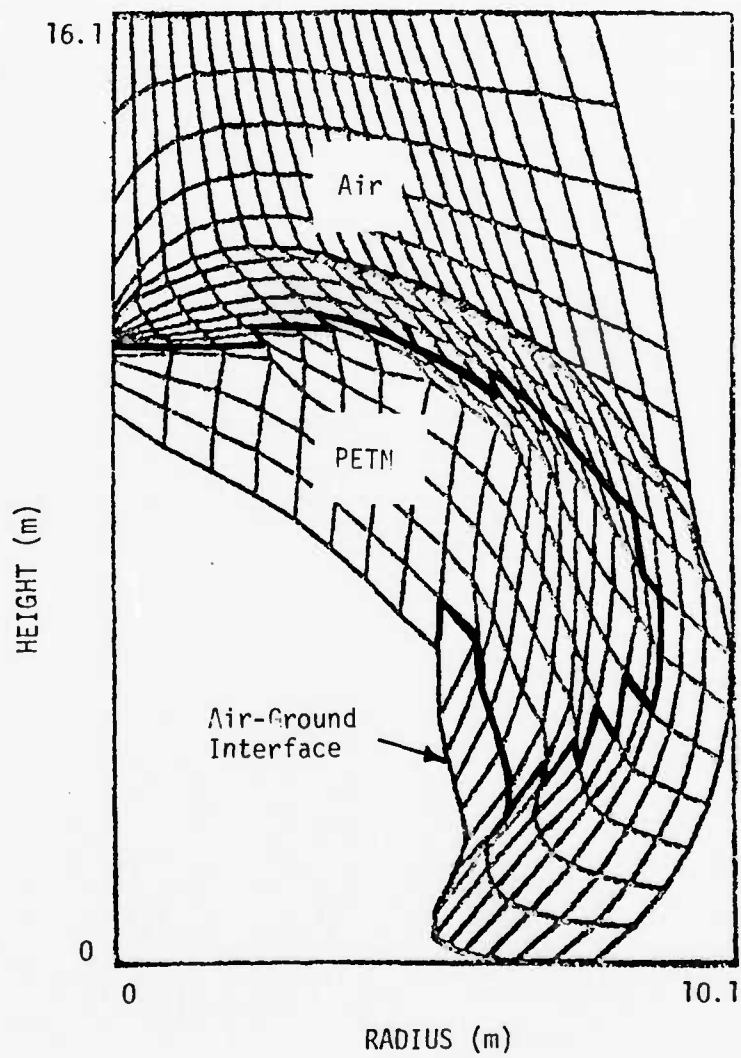
Figure 15. Final grid configuration and material
interfaces above the source.

40
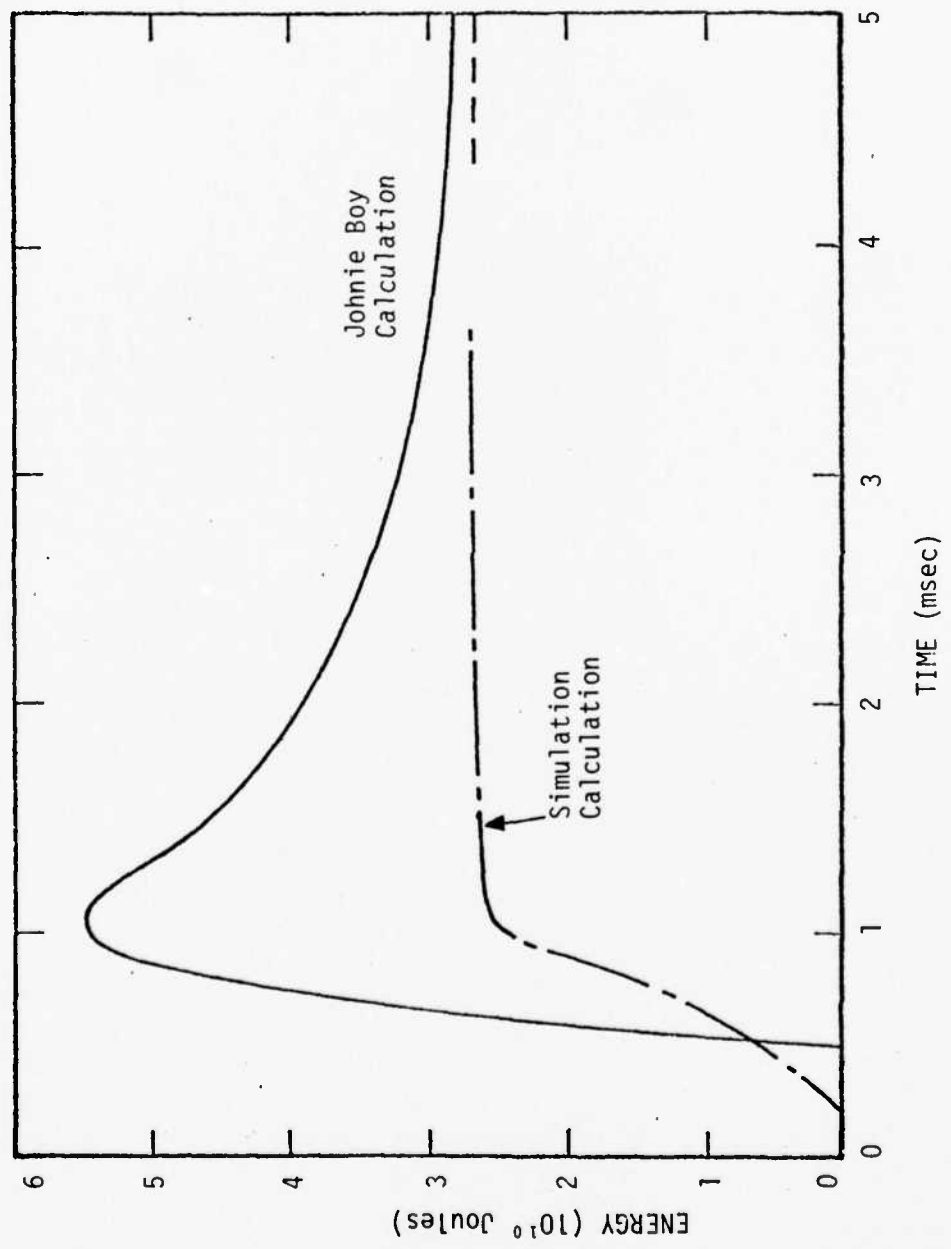
Figure 16. Kinetic energy coupling for final prediction.

41
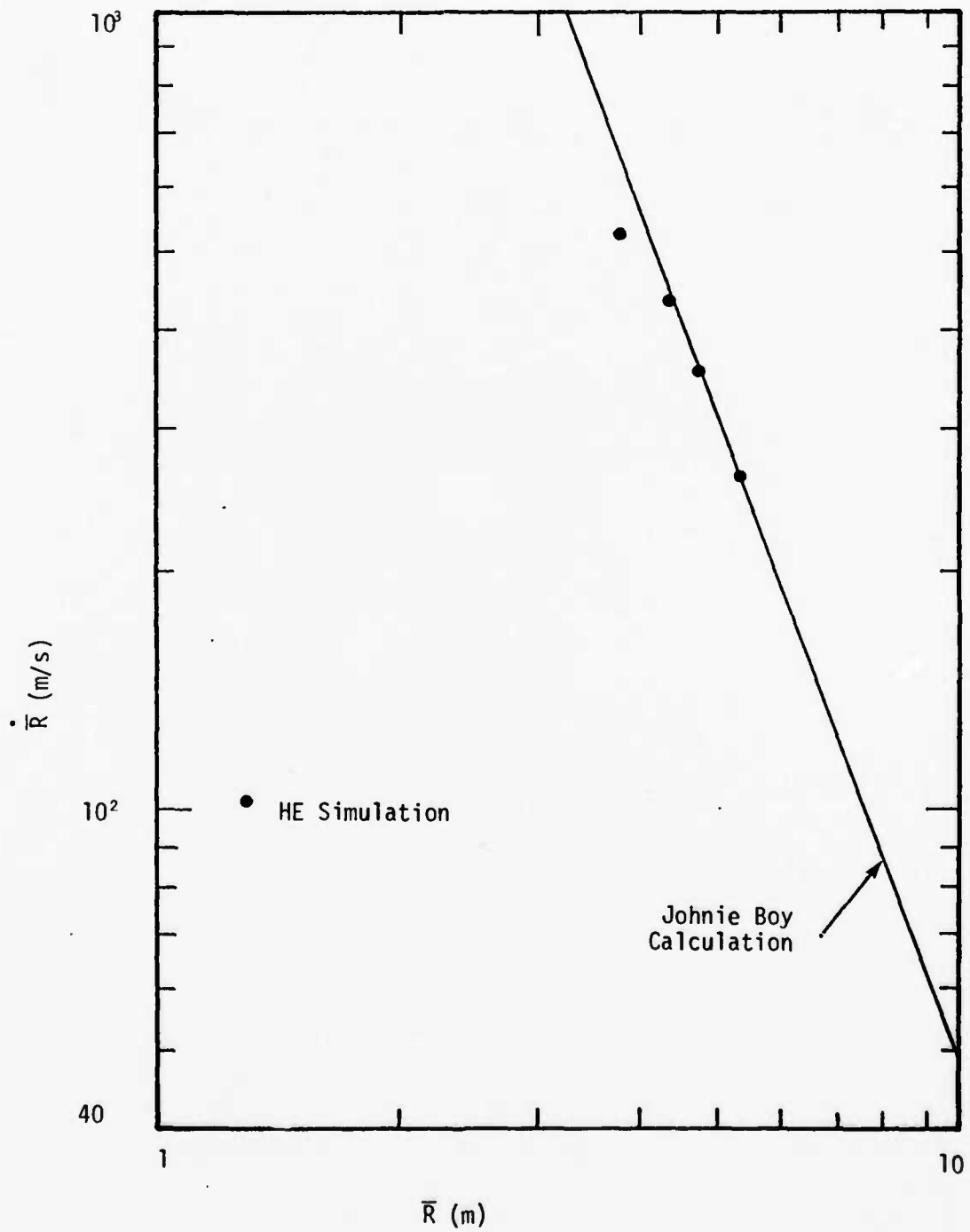
Figure 17. Comparison of reference surface motion.
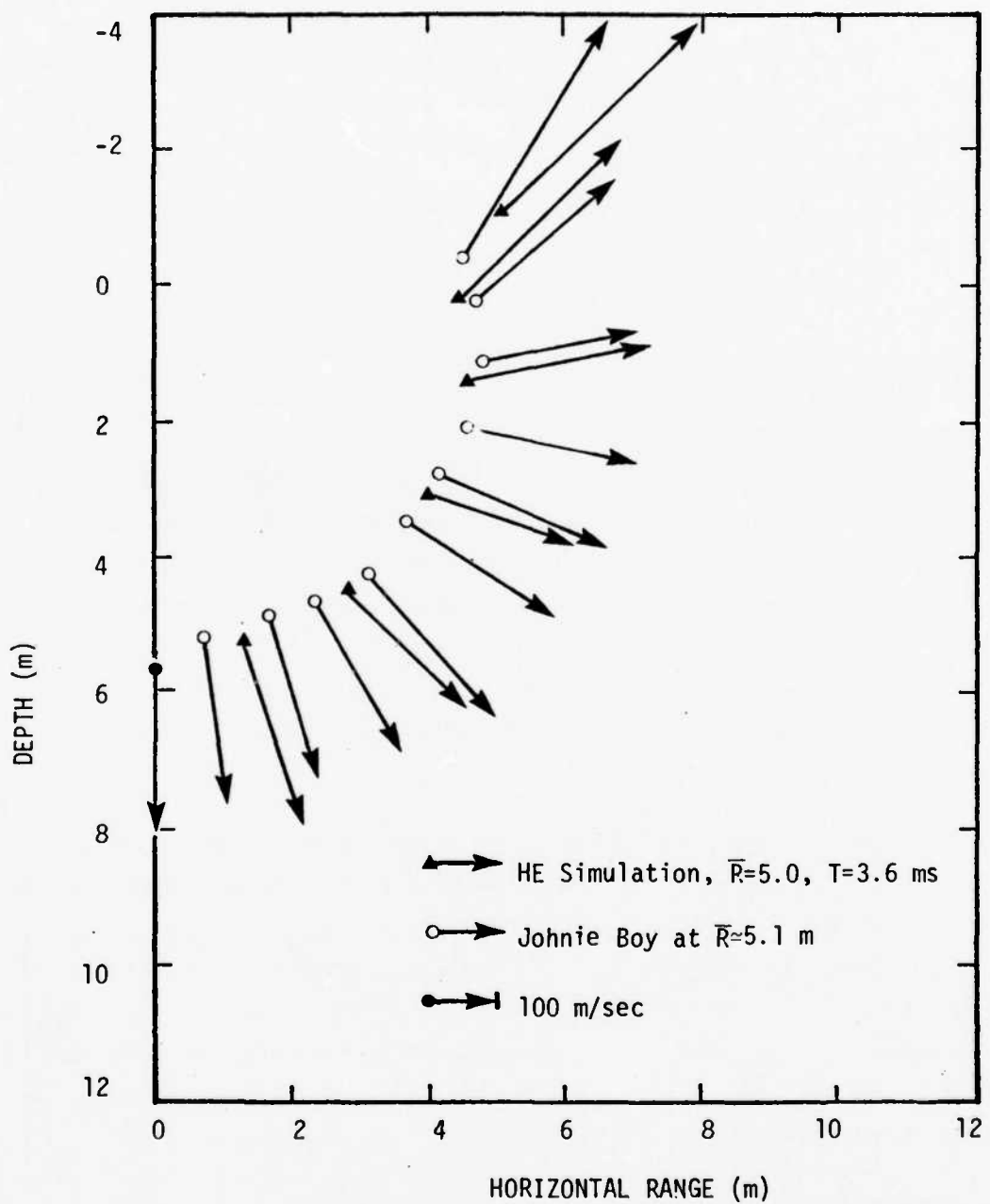
Figure 18. Comparison of reference surface motion.

comparison appears quite good.

The final step in defining the simulation event on the Boeing facility is to choose the gravitational acceleration to be used with one of the standard PETN charges that were available. The 1.2 gm charge was chosen which led to a value of g given by:

$$g = \left[\frac{4.93 \times 10^7 \text{gm}}{1.2 \text{ gm}} \right]^{1/3} = 345,$$

and the depth of burial should be $120/345 = 0.348$ cm.

3.4   SENSITIVITY STUDIES

Several additional calculations were run for a few miliseconds as we iterated on both high explosive yield and depth of burial to determine the best simulation charge. In the first series, the depth of burial of the high explosive was fixed at the center of the JOHNIE BOY source emplacement. Calculations were made with initial charge radii of 1.75, 2.2 and 2.57 m. The kinetic energy coupling beyond the 3.6 m reference surface is shown in Figure 19. The results indicate that the coupled energy increases more rapidly than a simple linear function of charge yield.

When we looked in more detail at the motion of the reference surface, it became clear that an increased burial depth for the high explosive would improve the simulation. The results of the two calculations at a depth of 1.2 m are shown in Figure 20. While these results suggest that the high explosive yield can be fine tuned to approximately ±10%, it is not as clear how well the "best" depth of burial can be determined. This choice hinges more on flow field comparisons such as those shown in Figure 18. We doubt that an increase in charge burial will improve this comparison to any marked degree.

3.5   COMPARISON WITH SIMULATION TEST RESULTS

The dimensions of the predicted simulation of JOHNIE BOY are compared with the Boeing test results in Table 4. The test JB1 was conducted at the suggested depth of burial of 0.348 cm (0.64 charge radii for the 1.2 gm charge) as accurately as possible. As a study of depth of burial sensitivity, the DOB

44
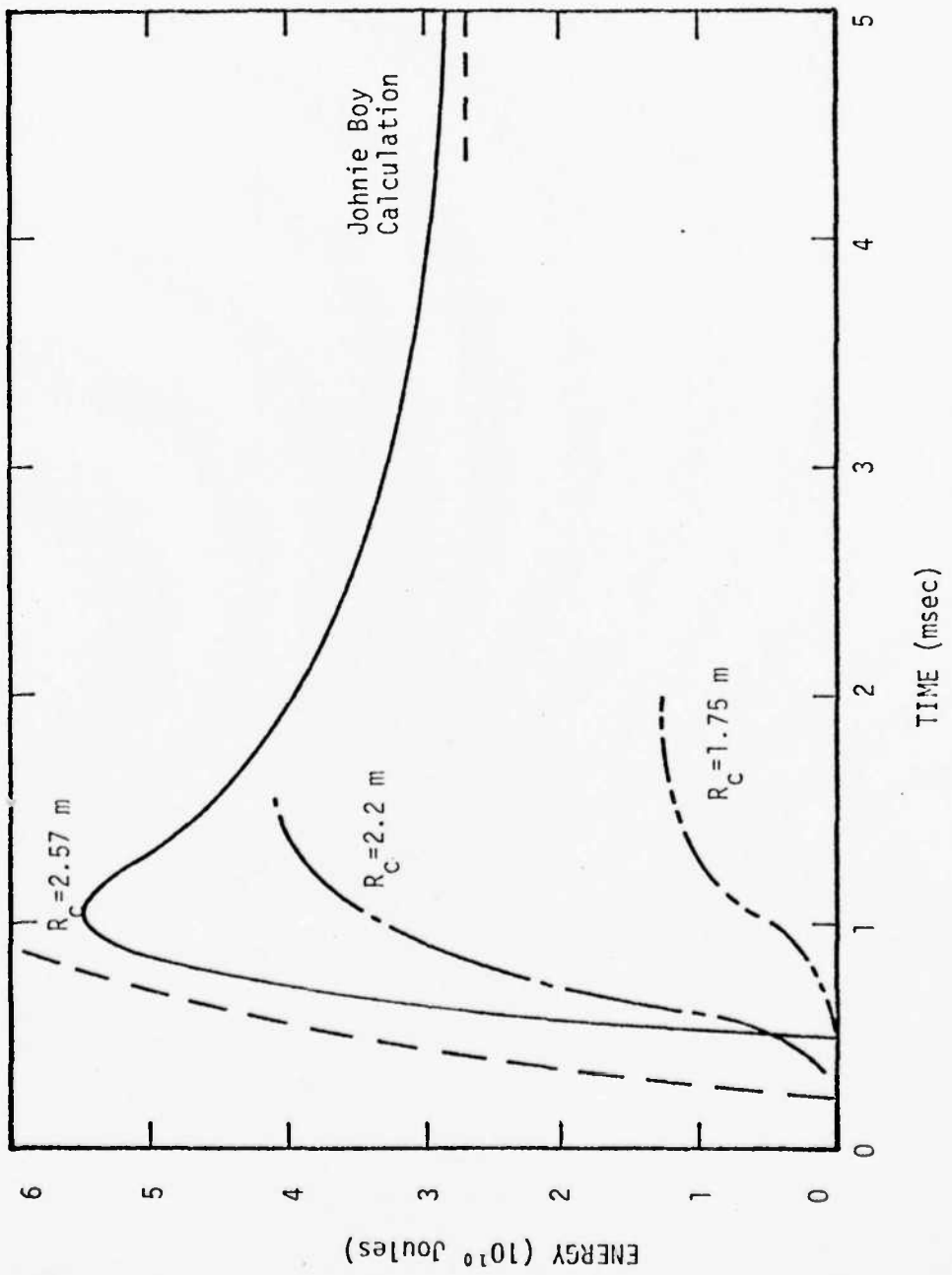
Figure 19. Effect of PETN charge size at 0.58 m DOB.
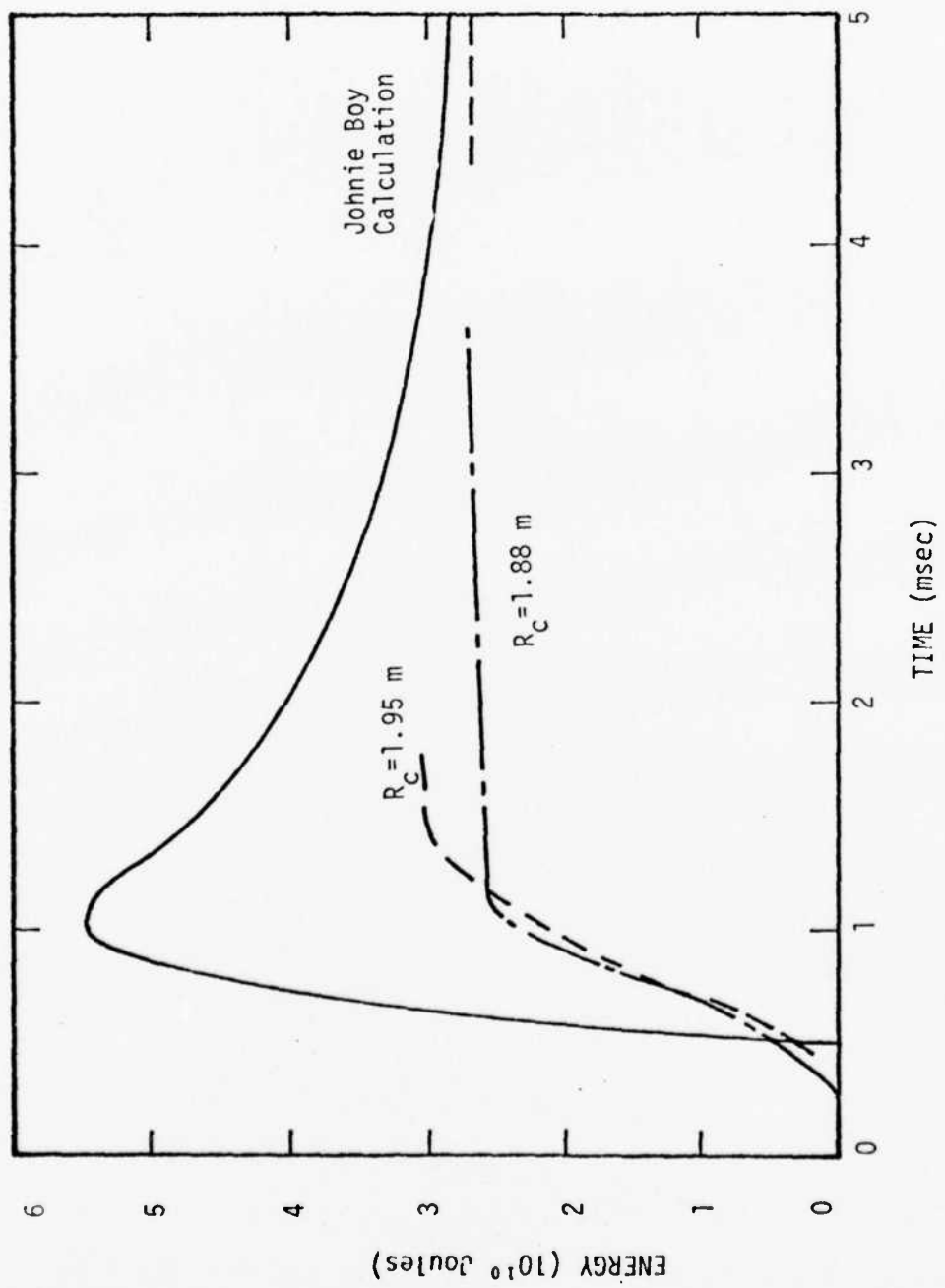
Figure 20. Effect of PETN charge size at 1.2 m DOB.

Table 4

Comparison of Simulation Crater Dimensions

	JOHNIE BOY*	JB1	JB2
Radius (cm)	5.39	5.37	6.08
Depth (cm)	2.70	2.26	2.76
Apparent Volume (cm^3	100.	77.7	116.
Aspect Ratio	2.0	2.38	2.2

---

*Scaled down by 345 in linear dimensions.

was increased to 1.47 charge radii for JB2. The effects of DOB variation are discussed in more detail in Section 4. We consider the simulation quite satisfactory considering the uncertainties we have already discussed.

We would like to emphasize once more the uncertainties which are likely to frustrate further refinement of this simulation. Measurements of density at the JOHNIE BOY site have varied from a low of 1.39 g/cm^3 to a high of 1.8 g/cm^3 and moisture content has shown a variation from 7.1 to 11.5%. It has been suggested[16] that the details of source emplacement can change the charge equivalence by 30%. The yield of the PETN charges, which we have suggested as a third source of uncertainty, could be better determined by further testing. Such tests should be conducted if only to establish the true TNT equivalence of these particular charges. In addition, the observed variation could be caused by a weak rate effect causing a deviation from true similitude in these small-scale tests.

4. ANALYSIS OF CENTRIFUGE CRATERING DATA

The purpose of this section is to analyze the centrifuge crater data obtained by Boeing in conjunction with preexisting data obtained at 1 g. We describe several systematic relations between dimensions of explosive craters produced by near-surface explosions and parameters of the explosion, such as yield and height of burst. This comparison demonstrates the power of the centrifuge approach, as well as providing potentially useful relations in its own right. Some of the systematic relations are expected from theoretical considerations, but others are purely empirical. It is hoped that the delineation of the empirical relations will stimulate theoretical analysis of the cratering process in order that their bases may be ascertained.

4.1 BACKGROUND

Earlier work by Cooper [41] has related the effect of height of burst on cratering efficiency (crater volume divided by explosive yield), and has achieved considerable success in synthesizing cratering data from a wide range of yields, explosive types and geologic media. Briefly, Cooper suggested that the apparent crater volume V_a produced by an explosion of yield Y could be expressed as

$$V_a = v(G,S,H) \times Y \tag{16}$$

where the cratering efficiency $v(G,S,H)$ is a function of the geology (G), the explosive source (S) and the scaled height of burst (H). The parameter used to scale the height of burst and other linear dimensions was chosen to be $V_a^{1/3}$ (i.e., $H = h/V_a^{1/3}$; h = height of burst). Cooper factors $v(G,S,H)$ into

$$v(G,S,H) = K(G)v_0(G_0,S)F(S,H) \tag{17}$$

where $v_0(G_0, S)$ is a "standard" cratering efficiency for source S at zero height of burst in a standard geology G_0, $K(G)$ is the ratio of the zero height of burst efficiency in geology G to that in G_0, and $F(S,H)$ is a height of burst shape factor for the source S.

Recently two series of very precisely controlled cratering experiments have been conducted which, when considered together, indicate a fundamental difficulty in the volume scaling analysis. Results of these experiments are

49

summarized in Tables 5 and 6. The first set of data, obtained by Piekutowski,[15] consist of a large number of cratering experiments in Ottawa sand using small (0.4 gm to 4 gm) high explosive spherical charges. Considerable effort was directed to producing precisely characterized and reproducible test beds. As a result, the data obtained were very reproducible. Piekutowski investigated the effects of charge type (PETN and $Pb(N_3)_2$ were used), height of burst and test bed bulk density. Observed cratering efficiencies were an order of magnitude higher than efficiencies obtained with 100 kg to 1000 kg explosive charges in natural sands such as alluvium.[42]

Schmidt[43] has conducted tests similar to those of Piekutowski, using 0.4 to 4 gm charges in Ottawa sand at zero height of burst, but at high acceleration in a centrifuge. His data, together with Piekutowski's, show that cratering efficiency decreases as the product $g^3 Y$ increases. Specifically,

$$v_o \propto Y^{5/6} / \sqrt{g} \qquad . \qquad (18)$$

Since yields of the Pacific cratering events are typically 3 or 4 orders of magnitude larger than those of Nevada events, application of Eq. (18) would indicate standard cratering efficiencies lower by a factor of $10^{1/2}$ to $10^{2/3}$ (3.2 to 4.6) ; hence, the data base was re-examined to see if use of Eq. (18) instead of Eq. (16) could lead to an improved predictive capability. Schmidt has also conducted a height of burst study at high g-levels in a reconstituted dry alluvium. These data are discussed in Section 4.3 of this report.

4.2   SCALING RELATIONS

Numerous scaling relations have been proposed for reconciling crater dimensions from tests at different yields and in different materials. A comprehensive review of them is not the object of this report. The interested reader is referred to the many published papers dealing with the subject.[2-9,12] The brief discussion here is based on a dimensional analysis by Schmidt.[44] He groups the variables into four dimensionless groups as follows:

$$\pi_1 = V \, W^{-1} \, \rho$$
$$\pi_2 = g \, W^{1/3} \, U^{-2} \, \delta^{-1/3}$$
$$\pi_3 = h \rho^{1/3} \, W^{-1/3}$$
$$\pi_4 = \rho \delta^{-1}$$

50

Table 5

Summary of UDRI and BAC Cratering Data in Alluvium

Test	Density (Mg/m³)	Charge Type	Charge Mass (kg)	TNT Equivalent (kg)	HOB (m)	Volume (m³)	Radius (m)	Depth (m)	Accel. (g's)
UDRI-1	1.62	PbN_6	1.7×10^{-3}	5.7×10^{-4}	0	5.87×10^{-5}	6.47×10^{-2}	1.85×10^{-2}	1
UDRI-2	1.58	PbN_6	1.7×10^{-3}	5.7×10^{-4}	0	7.24×10^{-5}	6.9×10^{-2}	1.95×10^{-2}	1
UDRI-3	1.60	PbN_6	1.7×10^{-3}	5.7×10^{-4}	0	4.50×10^{-5}	5.84×10^{-2}	1.75×10^{-2}	1
UDRI-4	1.57	PETN	1.25×10^{-3}	1.7×10^{-3}	0	1.03×10^{-4}	6.88×10^{-2}	2.4×10^{-2}	1
UDRI-5	1.55	PETN	4×10^{-3}	5.5×10^{-3}	0	1.96×10^{-4}	8.28×10^{-2}	2.86×10^{-2}	1
UDRI-6	1.58	PETN	4×10^{-3}	5.5×10^{-3}	0	1.75×10^{-4}	8.52×10^{-2}	2.80×10^{-2}	1
UDRI-7	1.59	PETN	1.25×10^{-3}	1.7×10^{-3}	0	6.66×10^{-5}	6.44×10^{-2}	2.0×10^{-2}	1
BAC-16-0	1.52 *	PETN	1.25×10^{-3}	1.7×10^{-3}	0	5.10×10^{-5}	4.78×10^{-2}	2.08×10^{-2}	451
BAC-16-X	1.52 *	PETN	1.25×10^{-3}	1.7×10^{-3}	0	4.81×10^{-5}	4.70×10^{-2}	1.91×10^{-2}	451
BAC-17-0	1.61	PETN	3.9×10^{-3}	5.4×10^{-3}	0	9.65×10^{-5}	6.23×10^{-2}	1.97×10^{-2}	306
BAC-17-X	1.61	PETN	1.25×10^{-3}	1.7×10^{-3}	0	3.02×10^{-5}	4.22×10^{-2}	1.35×10^{-2}	451
BAC-18-0	1.57	PETN	1.25×10^{-3}	1.7×10^{-3}	-3.62×10^{-3}	7.77×10^{-5}	5.37×10^{-2}	2.26×10^{-2}	345
BAC-18-X	1.58	PETN	1.25×10^{-3}	1.7×10^{-3}	-8.45×10^{-3}	1.16×10^{-4}	6.08×10^{-2}	2.76×10^{-2}	345

* Approximate density, original packing about 1.43 Mg/m^3, but ground zero surface settled prior to shot.

Table 6. Summary of UORI and BAC Cratering Data in Ottawa Sand

Test	Density (Mg/m^3)	Charge Type	Charge Mass (kg)	TNT Equivalent (kg)	HOB (m)	Volume (m^3)	Radius (m)	Depth (m)	Accel. (g's)
UDRI-9	1.80	PbN_6	1.7×10^{-3}	5.7×10^{-4}	0	4.36×10^{-4}	1.02×10^{-1}	2.29×10^{-2}	1
UORI-22	1.80	Pb''_6	1.7×10^{-3}	5.7×10^{-4}	0	4.19×10^{-4}	1.01×10^{-1}	2.35×10^{-2}	1
UDRI-107	1.80	PETN	4×10^{-4}	6×10^{-4}	0	2.59×10^{-4}	8.73×10^{-2}	1.97×10^{-2}	1
UDRI-117	1.81	PETN	4×10^{-4}	6×10^{-4}	0	2.74×10^{-4}	8.76×10^{-2}	2.06×10^{-2}	1
UDRI-120	1.79	PETN	4×10^{-4}	6×10^{-4}	0	2.92×10^{-4}	8.88×10^{-2}	2.13×10^{-2}	1
UDRI-146	1.81	PETN	4×10^{-4}	6×10^{-4}	0	2.84×10^{-4}	8.89×10^{-2}	2.02×10^{-2}	1
BAC-10-0	1.78	PETN	4×10^{-4}	6×10^{-4}	0	1.71×10^{-5}	3.56×10^{-2}	7.1×10^{-3}	463
BAC-10-X	1.77	PbN_6	1.7×10^{-3}	5.7×10^{-4}	0	2.71×10^{-5}	3.87×10^{-2}	8.9×10^{-3}	463
BAC-11-0	1.78	PETN	1.25×10^{-3}	1.7×10^{-3}	0	3.80×10^{-5}	4.31×10^{-2}	9.7×10^{-3}	451
8AC-11-X	1.78	PETN	1.25×10^{-3}	1.7×10^{-3}	0	3.51×10^{-5}	4.38×10^{-2}	9.9×10^{-3}	451
BAC-12-0	1.78	PETN	4×10^{-3}	5.5×10^{-3}	0	1.01×10^{-4}	6.41×10^{-2}	1.31×10^{-2}	451
BAC-12-X *	1.68	PETN	4×10^{-3}	5.5×10^{-3}	0	9.63×10^{-5}	6.33×10^{-2}	1.28×10^{-2}	451
BAC-13-0	1.78	PETN	4×10^{-3}	5.5×10^{-3}	0	1.25×10^{-4}	6.88×10^{-2}	1.37×10^{-2}	306
BAC-13-X *	1.68	PETN	4×10^{-3}	5.5×10^{-3}	0	1.19×10^{-4}	6.65×10^{-2}	1.56×10^{-2}	306
8AC-15-0	1.78	PETN	4×10^{-4}	5.5×10^{-4}	0	9.52×10^{-5}	6.40×10^{-2}	1.27×10^{-2}	10
BAC-15-X	1.78	PETN	4×10^{-4}	5.5×10^{-4}	0	9.48×10^{-5}	6.40×10^{-2}	1.26×10^{-2}	10

* Two high g tests used a finer grain size fraction of Ottawa sand which did not pack as tightly as the coarser material.

52

where

> V = crater volume
> ρ = medium density
> W = mass of charge*
> g = gravitational acceleration
> U = Chapman-Jouget particle velocity
> δ = Chapman-Jouget density
> h = height of burst.

The crater volume then is given by solution of $f_1(\pi_1, \pi_2, \pi_3, \pi_4) = 0$. For almost all materials, Schmidt considered that neither ρ nor δ varies by an appreciable amount, so that we can solve $f_2(\pi_1, \pi_2, \pi_3) = 0$. For the particular case of zero height of burst, π_3 = constant and we have $\pi_1 \pi_2^{\alpha}$ = constant

or

$$\frac{V\rho}{W} = \left\{ \frac{g}{U^2} \left(\frac{W}{\delta} \right)^{1/3} \right\}^{-\alpha} = \left\{ \frac{g^3 W}{U^6 \delta} \right\}^{-\alpha/3}. \tag{19}$$

Based on this analysis we expect that a plot of the log of the crater efficiency (V/W) against the log of $g^3 W$ will be a straight line of slope $-\alpha/3$ for tests with a given explosive. Data for dry Ottawa sand at 1g and at high g are shown in Figure 21. Over a range of almost nine orders of magnitude the value of α is determined to be about 1/2 when only data using PETN are considered. (The best fit is obtained with $\alpha = 0.478$.)

(It should be noted that the $\alpha = 1/2$ value indicates that $V/Y^{5/6}$, rather than V/Y, should be used when comparing craters produced by quite different yields. Thus, Eq. (16) should be modified to be

$$V_a = v (G,S,H) \times Y^n \tag{20}$$

where V_a is the efficiency in units of volume/(yield)^n instead of Cooper's volume/-yield and n=5/6. We shall return to a discussion of this $Y^{5/6}$ dependence when discussing height of burst effects in Section 4.3)

---

*When considering a single type of explosive, W and Y are interchangeable. However, such is not the case when comparing different explosives.
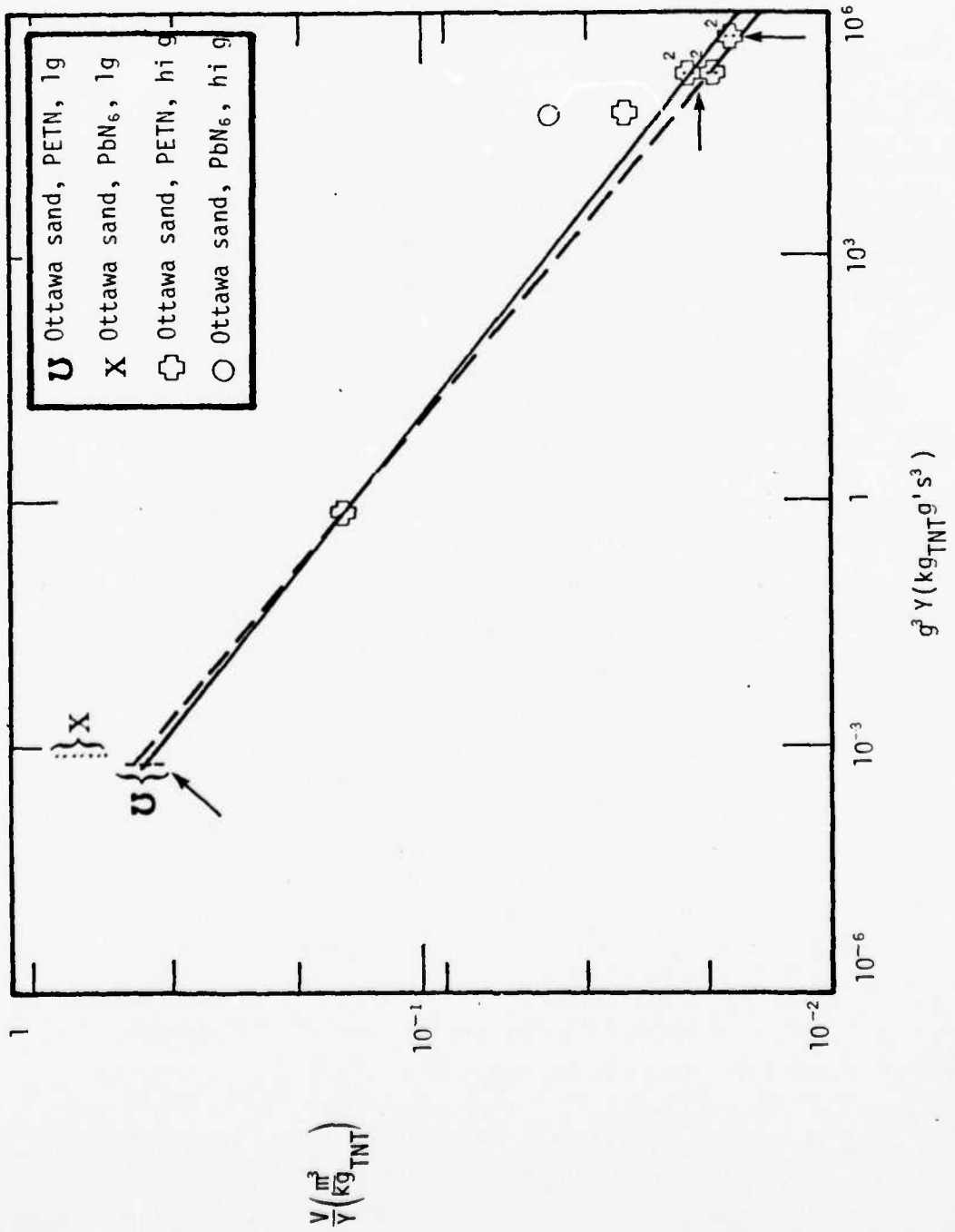
Figure 21. Crater efficiency in small scale explosive tests by Piekutowski (15) and Schmidt (43). Solid line is fit to data indicated by arrows (slope= $-\frac{1}{6.27}$). Dashed line has slope $-\frac{1}{6}$.

The effect of changing the type of explosive is also readily seen in Figure 21. Charges of PETN used actually contain over 0.1 gram of AgN_3 as an initiator. This has little effect on 4 gram and 1 gram charges, but constitutes an appreciable amount of the charges equivalent to 0.4 grams of PETN. The high g data at $g^3Y = 10^5 (kg_{TNT} g's^3)$ were obtained using the same 0.4 gram PETN charges and are seen to lie significantly off of the line of the other PETN data. In addition, both high g and low g tests were conducted using $Pb(N_3)_2$ charges of the same TNT equivalence as the PETN charges. $Pb(N_3)_2$ is apparently 50% more efficient in cratering than is PETN for a given energy content.

In order to quantify the effects of changing explosive type, we can look at the relation $\pi_1 \pi_2^{\alpha}$ = constant. In particular the π_2 term contains information on the C-J state of the explosive. So if we plot π_1 versus π_2, instead of just V/Y versus g^3Y, we would expect data for all explosives to lie on a single line. Using the explosive properties in Table 7, we find that this is indeed the case for Ottawa sand, as illustrated in Figure 22. Hence, by using the entire π_2 term, we can bring all the data for Ottawa sand at a density of 1.78-1.80 Mg/m^3 onto a single line. (The effect of AgN_3 initiators is still seen because the initiator was not included in describing the C-J state.)

Cratering data from alluvium, playa sand and other soil media[15,42,43] are presented in Figure 23 in the form of a π_1-π_2 plot. Included are Schmidt's data obtained at 300 to 450 g's and Piekutowski's at 1 g in reconstituted Kirtland AFB alluvium. With the exception of the PACE tests, a series of 1000 lb. shots in saturated, unconsolidated coral sand, the data can be fit to a single straight line with a standard deviation of only 36% in crater volume. The line shown in the figure has the equation

$$V = (0.062\pm0.022 \ m^3)W^{0.977}g^{-0.070}\rho^{-1}\left(\frac{U^6\delta}{U^6_{TNT}\delta_{TNT}}\right)^{0.023} \qquad (21)$$

where W is the charge mass in kg, g is in g's, ρ is in Mg/m^3 and U and δ are in

55

Table 7

Properties of Explosives

Explosive	Energy Equivalence (TNT = 1.0)	C-J Density δ (Mg/m^3)	C-J Velocity U (km/s)	U$^6\delta$	Reference
TNT	1.0	2.16	1.67	46.9	(40)
PETN	1.37	.2.45	2.33	392	(40)
Pb (N$_3$)$_2$	0.33	4.89	0.96	3.83	(45)
C-4	1.09	2.13	2.03	149	(40)
ANFO	1.14	1.24	1.49	13.6	(16)

℧ Ottawa sand, PETN, 1g

X Ottawa sand, PbN$_6$, 1g

○ Ottawa sand, PbN$_6$, hi g

✣ Ottawa sand, PETN, hi g

$\dfrac{\rho V}{W}$

10^3

10^2

10^1

slope $= -\dfrac{1}{6.27}$

slope $= -\dfrac{1}{6}$

10^{-5} 10^0 10^5

$g^3 W \left\{ \dfrac{u^6_{TNT} \delta_{TNT}}{u^6 \delta} \right\} (g's^3\,kg)$
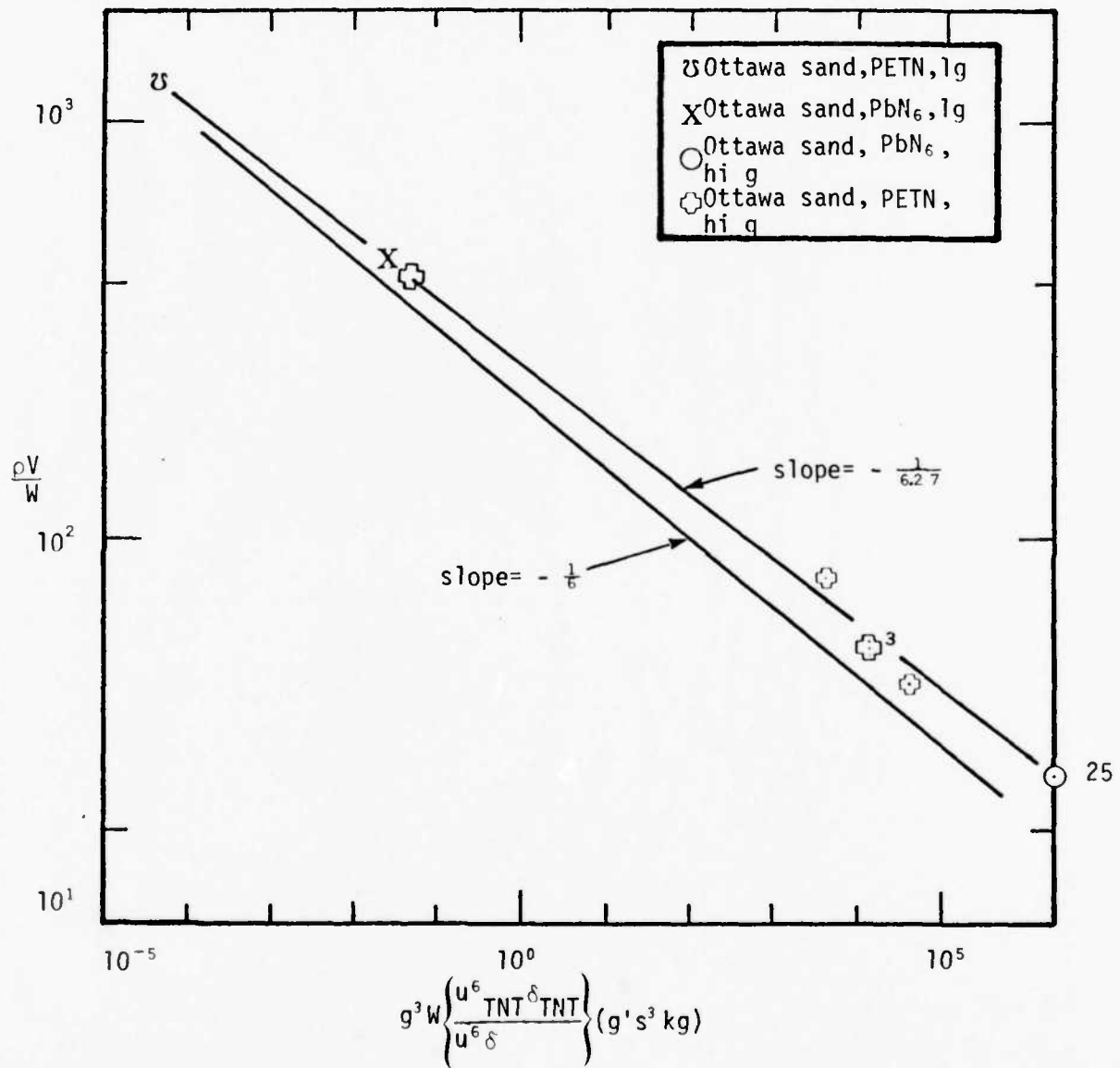
Figure 22.   Relation of π_1 to π_2 for tests in Ottawa
sand.

57
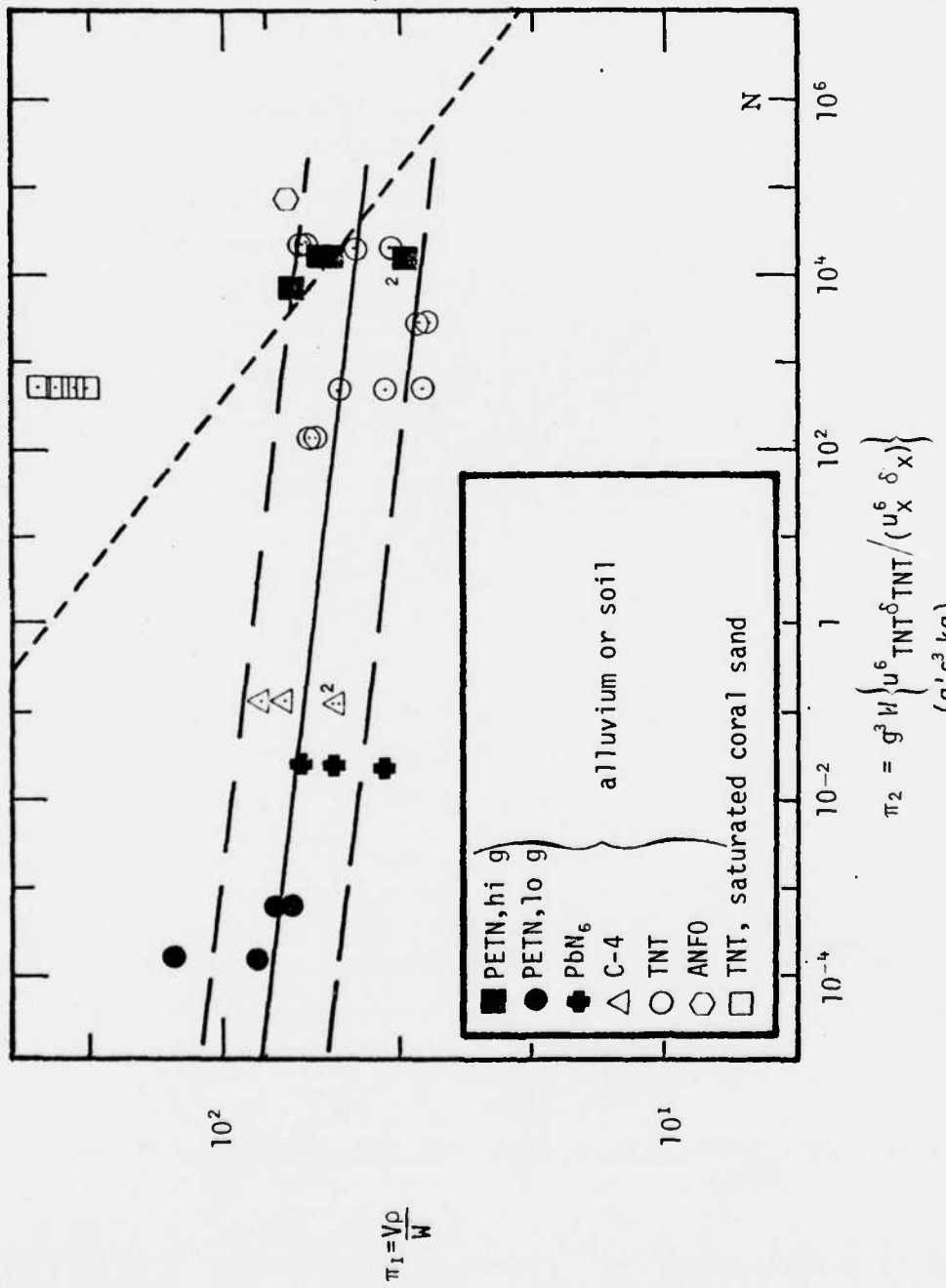
Figure 23. π_1-π_2 plot for craters in alluvium, soil and saturated coral sand. Dash line is best fit to data for Ottawa sand shown in Figure 22.

58

any consistent units. These tests encompass charges from less than a gram to 40 tons and media with densities from 1.13 to 1.70 Mg/m^3. In view of this wide diversity, the narrow scatter of the data is remarkable.

All of the soils that fit Eq. (21) are at least moderately cohesive. It is, therefore, possible that the difference in behavior of these soils from that of Ottawa sand is due to their cohesive nature which inhibits cratering at low yields. It is perhaps significant that the cohesion of the KAFB alluvium, about 1.5×10^5 Pa (43, App.E), is approximately equal to the initial overburden stress ($\rho g d$) at the bottom of the crater, $1-1.4 \times 10^5$ Pa. We expect that at still larger scaled yields, the effect of cohesion would disappear and crater trends should parallel those of Ottawa sand. For more cohesive materials this change should occur at even higher yields.

In view of our ultimate goal of understanding kiloton and megaton nuclear craters, we feel it is necessary to speculate on the trend which might be followed by craters in alluvium at still higher yields. It is reasonable to expect that cohesion could decrease cratering efficiency since more work must be done to expand a cohesive material than a non-cohesive one. However, it is difficult to see how cratering efficiency could ever be higher in a cohesive material than in an otherwise similar non-cohesive material. That being the case, we should expect that at high yields the cohesive material would exhibit the same $Y^{-1/6}$ dependence of cratering efficiency on yield as is seen in the non-cohesive medium. However, the existing data are insufficient to determine where this change from $Y^{-0.02}$ to $Y^{-1/6}$ should occur. The presently available tests extend only up to the intersection with the Ottawa sand trend. Unfortunately, that is not necessarily an upper limit. The PACE tests indicate that higher efficiencies are possible in wet media. A centrifuge test with a 1.7 gram $Pb(N_3)_2$ charge at 500 g's would be most helpful in this regard since it would have π_2 equivalent to about 5×10^6 kg of TNT.

If the above comments are valid, it will be difficult to apply a single factoring approach as used by Cooper (e.g., Eq. (17)) over the entire range of yields, but at high yields, if all media trend as $Y^{-1/6}$, then the factoring approach

should apply and Eq. (16) can be rewritten

$$V = K(G)v_o(S)F(H,S)\eta(Y) \tag{22}$$

where $K(G) \propto 1/\rho$, $v_o(S) = (U\delta^{1/6})/(\epsilon^{5/6}U_{TNT}\delta^{1/6}{}_{TNT})$, and $\eta(Y) = Y^{5/6}\sqrt{g}$. $F(S,H)$ is a height of burst function discussed in Section 4.3, and ϵ is the ratio of the specific energy to that of TNT.

It is difficult to apply Eq. (21) to nuclear cratering events since the C-J state cannot be defined. However, noting the Eq. (22) factors, we can still plot the nuclear data as though it were an energy equivalent mass of TNT. In Figure 23, we have indicated by a N the interpolated, zero height of burst, 1 kt nuclear crater of Vortman.[12] Based on this point, we see that $v_o(S) \sim 5.0$ relative to the Ottawa sand line or, as an inferred upper limit $v_o(S) \sim 7.0$ relative to the low yield alluvium line. This compares with a value of 7.35 obtained in the previous section of this report by entirely different means. We will return to this point after discussing height of burst effects.

4.3   HEIGHT OF BURST EFFECTS

In order to discuss height of burst effects it is necessary to have a rational method to adjust heights for tests at different yields. Since the dimensions of volume are the cube of the dimensions of length, Cooper used the cube root of the crater volume to scale height of burst. One result of such a scheme is shown in Figure 24. (The raw data from nuclear tests Nevada, plotted as X, have been adjusted by a factor of 3.4 to the points □ to account for differences in the media.) Cooper's interpretation is that the tank shots behaved in a manner similar to the "low energy density" Nevada events whereas the other shots exhibited a markedly different height of burst effect because they were "high energy density" sources. (The ZUNI crater (▲), which partially overlapped earlier craters, is anomalous.) The slope of the "high energy density" curve far above the interface is nearly identical to that of the low energy density curve. There is no data base on which details of the curvature of the high energy curve can be evaluated. Hence, it is difficult to use this scheme to correct the high yield Pacific events to a zero height of burst.

We saw in Section 4.2 that the crater volume in sand varies as $Y^{5/6}$. That being the case, it is reasonable to replace $V^{1/3}$ by $(Y^{5/6})^{1/3} = Y^{5/18}$ as

60

"Normal" Pacific tests

Water tank shots

Zuni

Low yield alluvium events

Same as X but corrected for material

● ◆ ▲ X □

$\frac{V}{Y}\left(\frac{m^3}{kt}\right)$

10^5

10^4

10^3

$\frac{HOB}{Y^{1/3}}$

-0.15   -0.10   -0.05   0   0.05   0.10
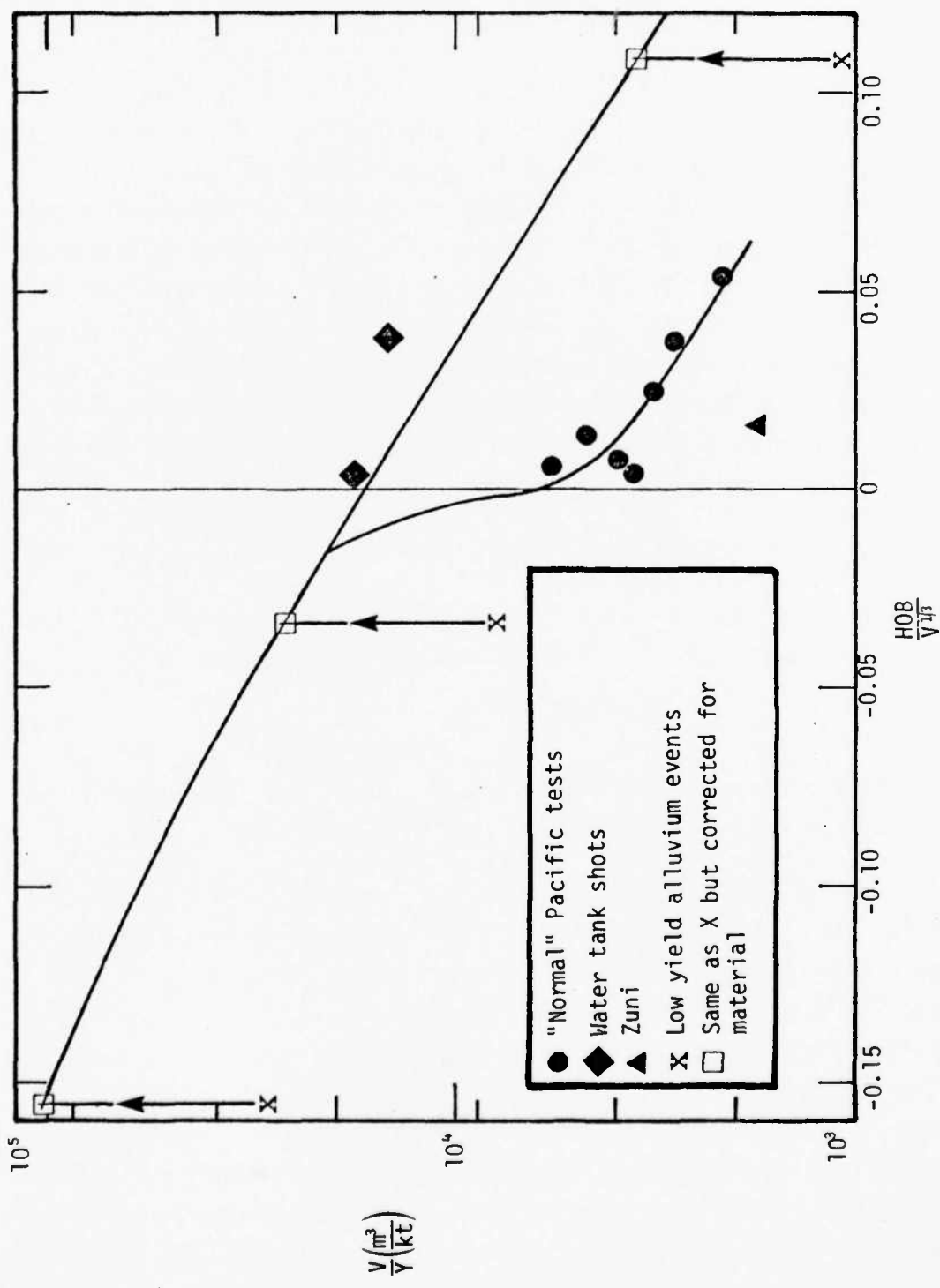
Figure 24. Volume cube root scaling of nuclear craters from Nevada and the Pacific Proving Ground.

61

the parameter for scaling linear dimensions. Thus, the scaled height of burst would be $HOB/Y^{5/18}$. If we plot $V/Y^{5/6}$ vs. $HOB/Y^{5/18}$, we should be able to determine the effect of height of burst on crater size for craters from a wide range of yields, as in Figure 25. Here we see that the "high energy density" events fall on the same curve as the Nevada events. (The line is a least squares fit to the eight "high energy density" points without the Nevada data.) As before, the two tank shots are anomalous, but they do represent the same slope as the rest of the data. The scatter of data about the curve in Figure 25 is greater than in Figure 24, but the fact that all normal nuclear sources (i.e., not tank shots) fit a single curve is a decided advantage. The deviations are, to some extent, systematic as will be discussed below. The greatest advantage of using Figure 25 instead of Figure 24 is that the intercept of the height of burst curve with zero height of burst is well defined. For absolute heights of burst less than 1 $m/kt^{5/18}$ the crater volume will be given by

$$V = V_o Y^{5/6} 10^{-0.49(H/Y^{5/18})}$$ (23)

where V_o is the volume of a nuclear crater at zero height of burst and a yield of 1 kt, and Y is in kilotons. By contrast, Figure 24 would give

$$V = V_o Y \ 10^{-6.6(HOB/V^{1/3})}$$ (24)

which is valid only for $0 < HOB/V^{1/3} < 0.02$ which includes only half of the Pacific events and is not valid for any negative heights of burst.

The PACE series of 1000 lb. TNT events conducted at the Pacific Proving Ground permit a direct comparison of nuclear and high explosive height of burst effects. Figure 26 shows the effect of height of burst on cratering efficiency for both $V^{1/3}$ scaling and $Y^{5/18}$ scaling. The curves labeled B and C and labeled E are taken from Figures 24 and 25, respectively, with extensions at depth of burst to include JANGLE U. Curves A and D, respectively, are indicative of the slope of the $V^{1/3}$ and $Y^{5/18}$ height of burst curves for high explosive as they cross zero height of burst. The slopes of the various curves at zero are given in Table 8 along with their intercepts. We note that the slope of the nuclear curve is 4.27 times that of the high explosive curve for $Y^{5/18}$ scaling.
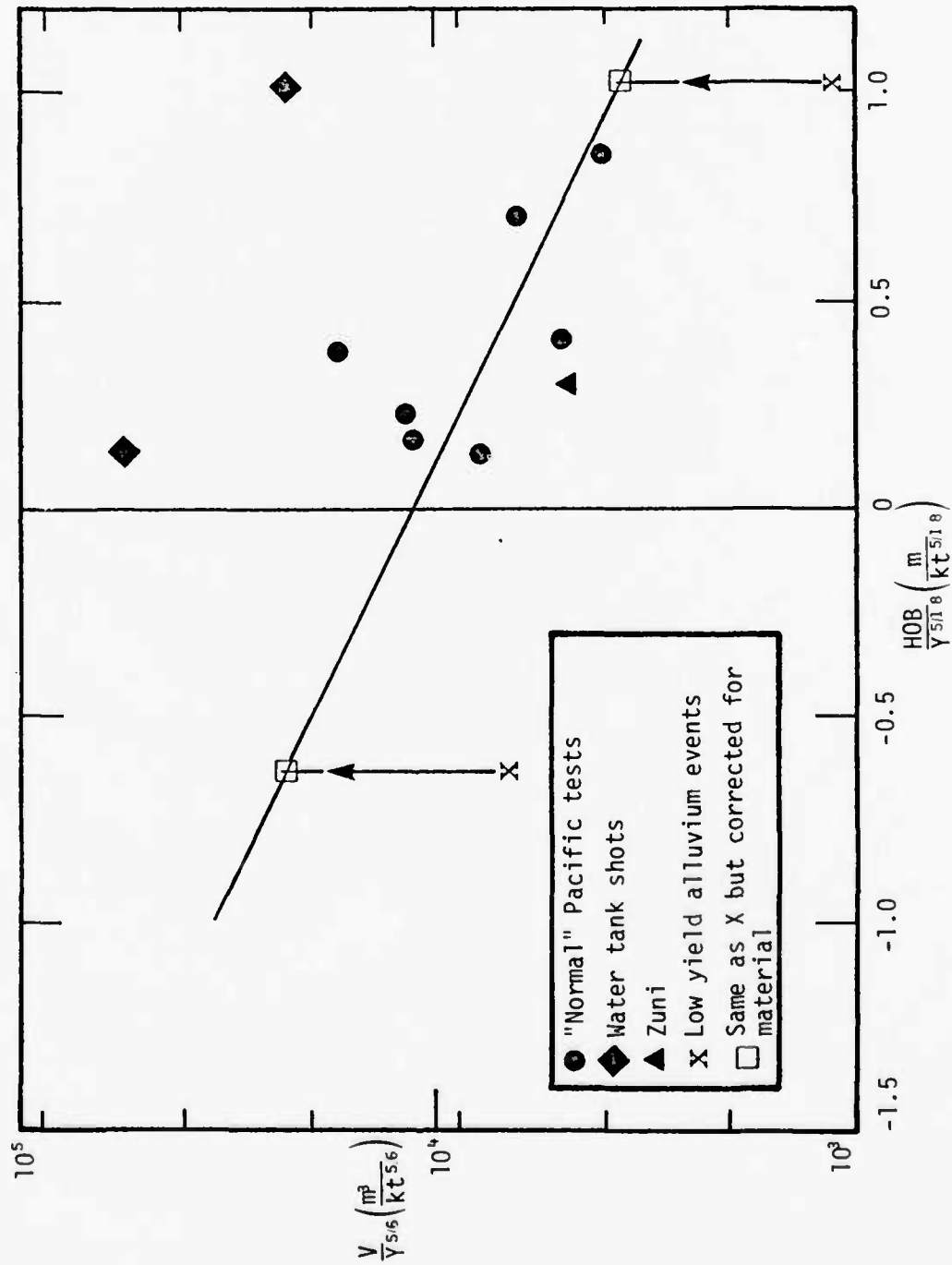
Figure 25. $Y^{5/18}$ scaling applied to height of burst effects for nuclear events.

63
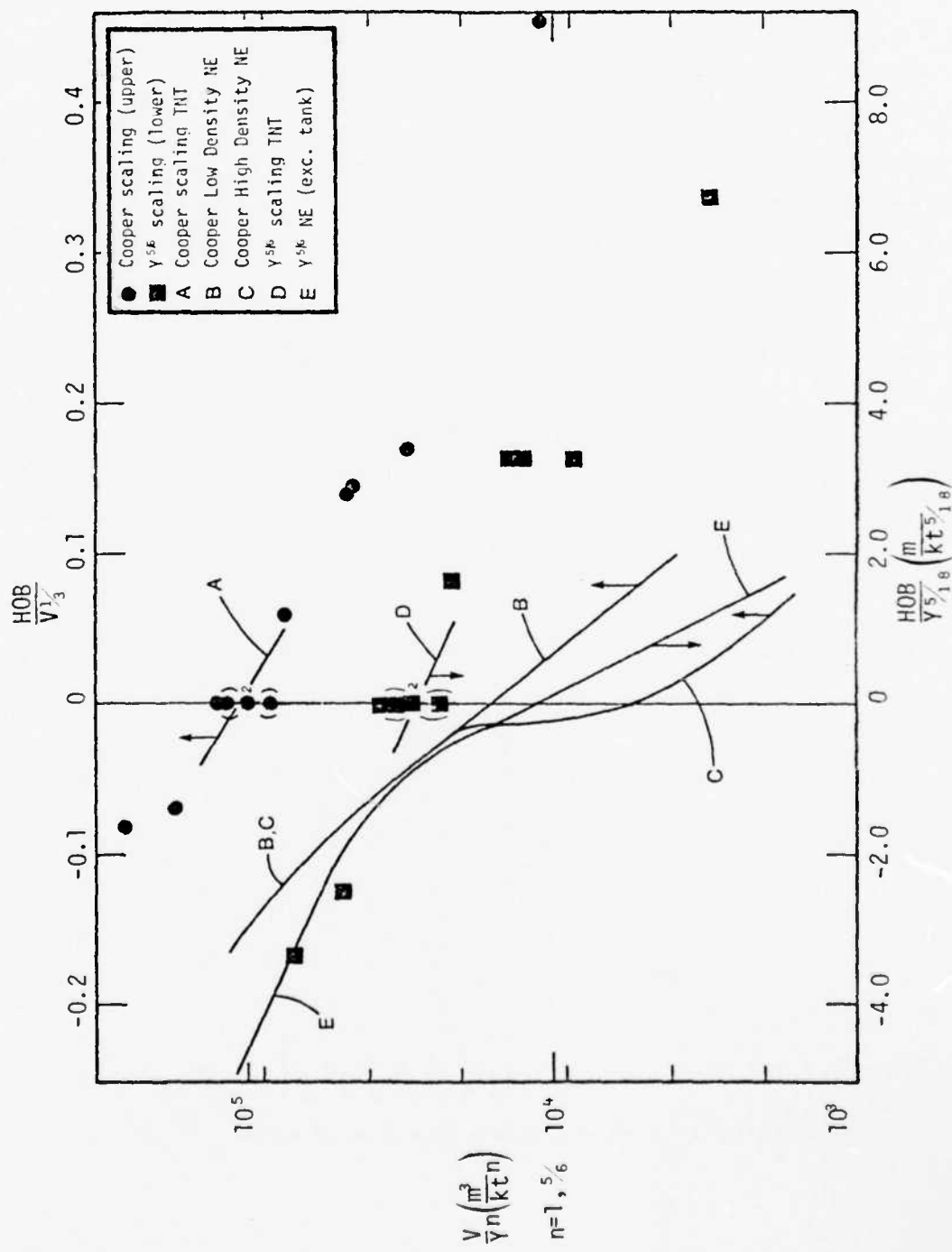
Figure 2b. Height of burst curves for nuclear and high explosive events.

64

Table 8
Relation of Height of Burst to Efficiency

Curve	$\dfrac{d\ (\log_{10} V/Y^n)}{d\ (\text{scaled HOB})}$	V/Y^n @ HOB = 0
B	- 6.60	1.58×10^4
C	-40.5	5.62×10^3
E	- 0.492	1.15×10^4
A	- 3.08	1.09×10^5
D	- 0.115	2.79×10^4

Hence,

$$V = V_o Y^{5/6} 10^{-0.115(H/Y^{5/18})}. \tag{25}$$

We are now in a position to use curve E to correct for height of burst effects and determine the effect of yield on crater efficiency for Pacific nuclear tests. This is done in Figure 27. It can be seen that there is considerable scatter, but the least squares line through the data has a slope of -.152, very nearly the value of -.159 observed in Ottawa sand. We can also determine the source effect for nuclear sources versus TNT sources in wet coral sand. Extrapolating to 1000 lb., we see that TNT is 2.75 times as effective as a nuclear device at zero height of burst (i.e., $v_o(S) = 2.75$). This is 40% to 60% lower than the value obtained by comparing craters in alluvium. However, in view of the scatter of the Pacific data, the difference may not be significant.

We can use Schmidt's tests 18-0 and 18-X to evaluate height of burst effects in alluvium. Based on these two tests alone, the slope similar to the values listed in Table 8 of a HOB-efficiency curve is -0.133, nearly identical to that of curve D in the PACE series. This agreement leads us to conclude that the two tests exhibit a high degree of internal consistency. The reproducibility of crater volume at zero height of burst is discussed in Section 4.4.

4.4 PREDICTING CRATER VOLUMES

The relations derived in the last two sections can be used to predict crater volumes to be expected from spherical explosions. As an example, consider that one wishes to predict the crater volume from a 1.25 gram PETN sphere in alluvium (density 1.57 Mg/m^3) with a height of burst of -0.64 charge radii at 345 g's. (This is, of course, Schmidt's 18-0 test.) Using these values, plus C-J data from Table 7, we use Eq. (21) to get an expected volume at zero height of burst of 42.5 ± 15 cm^3. Then applying a height of burst correction as in Eq. (25) we get an expected buried volume of 55 ± 20 cm^3.

This does not compare very favorably with the observed volume of 78 cm^3. However, the scatter between shots 16 and 17 by Schmidt is as large as the scatter among many alluvium shots. If, however, we use shot 16-0 or 16-X,
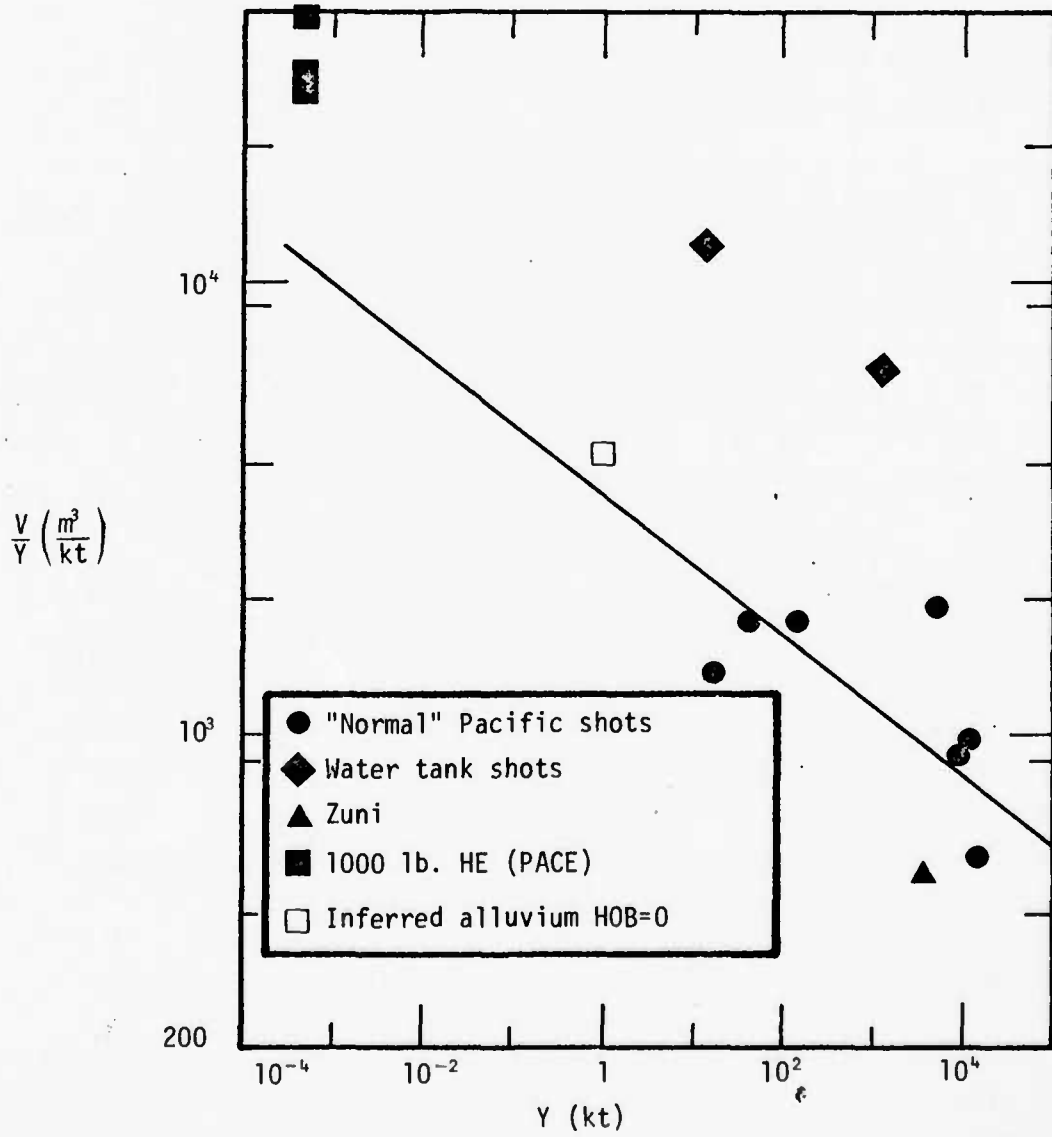
Figure 27. Effect of yield on crater efficiency for nuclear tests with height of burst adjustment.

Legend:
- ● "Normal" Pacific shots
- ◆ Water tank shots
- ▲ Zuni
- ■ 1000 lb. HE (PACE)
- □ Inferred alluvium HOB=0

Axis labels: $\frac{V}{Y}\left(\frac{m^3}{kt}\right)$ (vertical), Y (kt) (horizontal)

the zero height of burst volume would be about 54 cm^3, giving a buried value of 70 cm^3, virtually identical with that observed. This illustrates the difficulty caused by variable material properties in cratering experiments. The techniques used to prepare the test bed in each set of shots – (16-0 + 16-X), (17-0 + 17-X) and (18-0 + 18-X) – were slightly different. The bulk density was 1.52 Mg/m^3 fr 16-0 and 16-X, 1.61 Mg/m^3 for 17-0 and 17-X and 1.57 Mg/m^3 for 18-0 and 18-X.

The internal consistency of the two events 18 can be checked by using Eq. (25) to compare their observed volumes. The difference in scaled height of burst of the two events was 1.28 m/kt$^{5/18}$ (18-0 was at 0.64 charge radii and 18-X was at 1.47 charge radii, both below the surface.) Hence, we would expect that

$$\frac{V_{18-X}}{V_{18-0}} = 10^{0.115(1.28)} = 1.40 \ .$$

The observed volumes were 78 cm^3 and 116 cm^3 in a ratio of 1.49, only 6% higher than anticipated. Hence, we conclude that the tests 18 are consistent with other height of burst data from high explosive tests. Crater volumes for each set of tests by Schmidt were highly reproducible although they differed from set to set by as much as 45%. Collection of useful data in centrifuge cratering tests will depend on very careful attention to sample preparation. Consistency observed within a set of data indicates that reproducible materials can be obtained for a given sample preparation technique.

4.5. OTHER CRATER MEASURES

In order to use predicted crater values for targeting or vulnerability considerations, it is necessary to predict crater radii since that is the basis of most crater related vulnerability measures. Two measures of crater shape are useful in this regard – the aspect ratio, R/d, where R is the apparent crater radius and d is the apparent crater depth, and the shape factor, $F = V/(\pi R^2 d) = V(R/d)/\pi R^3$. Our discussion will involve mainly the aspect ratio, although a few thoughts are directed toward the shape factor.

A cursory glance at data for R/d from Ottawa sand, wet coral sand, and simulated alluvium with high explosive and alluvium with nuclear explosives indicates that the aspect ratio varies markedly from one material to another, and also with height of burst. If the aspect ratio is plotted against scaled height of burst for a given set of data, a straight line can be fit for absolute heights of burst less than 7 $m/kt^{5/18}$. The intercept of this line with zero height of burst is then taken as the reference aspect ratio for that data set, $\overline{(R/d)}_o^X$ for data set x. Values of $\overline{(R/d)}_o^X$ obtained in this way are given in Table 9.

The effect of yield or $g^3 Y$ on $\overline{(R/d)}_o^X$ is negligible. The mean of 7 high g tests in Ottawa sand at zero height of burst was 4.50 which is only 11% higher than $(R/d)_o^{UDRI}$ listed in Table 9. That variation is less than one standard deviation from the overall reduced aspect ratio versus scaled height of burst curve derived below.

In order to consider R/d data from several environments, we introduce the reduced aspect ratio defined as

$$\left(\frac{R}{d}\right)_{HOB}^R = \left(\frac{R}{d}\right)_{HOB}^X \frac{\overline{(R/d)}_o^{NE,al.}}{\overline{(R/d)}_o^X} \quad . \tag{26}$$

Thus, all aspect ratios are converted to values consistent with nuclear explosives in alluvium. When reduced aspect ratio is plotted against scaled height of burst, the data fall into a single scatter band. Fitting a straight line to all of the data at once, we find that there is a weak dependence of $(R/d)_{HOB}^R$ on height of burst. Specifically,

$$(R/d)_{HOB}^R = 2.35 \times 10^{0.021(HOB/Y^{5/18})} \pm 0.055 \tag{27}$$

where the indicated uncertainly is one standard deviation. This line is shown in Figure 28 along with the data.

Table 9

Zero Height of Burst Aspect Ratio of Various Crater Data Sets

| Date Set	Aspect Ratio (R/d)
Nuclear, alluvium	2.35
Boeing, alluvium	2.60
PACE, coral sand	2.77
UDRI, Ottawa sand	4.07
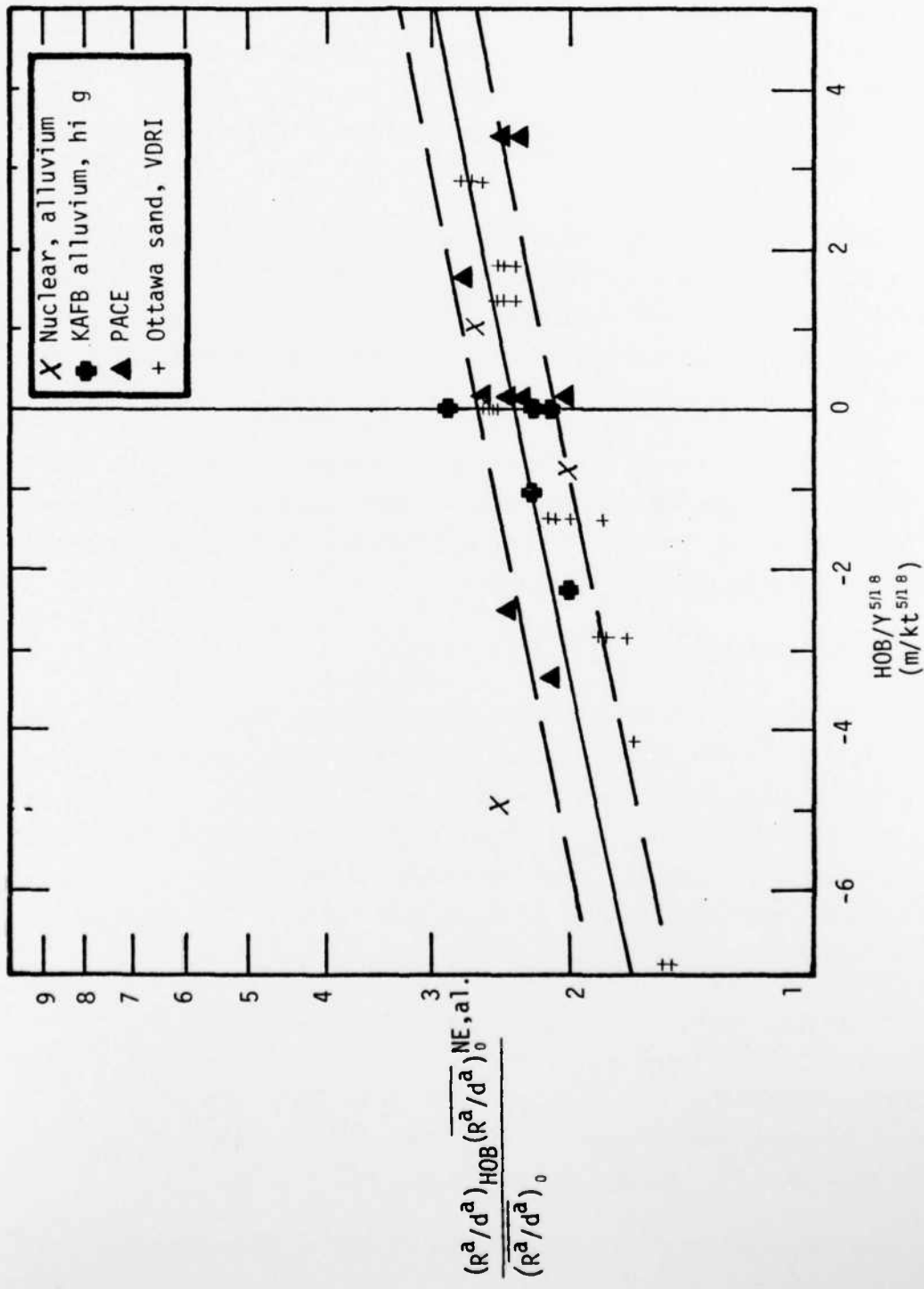
Figure 28. Reduced aspect ratio as a function of scaled height of burst.

71

An attempt to apply Eq. (27) to Pacific nuclear events will not be successful as is illustrated in Figure 29. The line and error band from Figure 28 are included along with data from JOHNIE BOY and JANGLE S. Only two Pacific events, CACTUS and LACROSS, are consistent with any of the other data. Recall that the PACE series, which were 1000 lb. TNT tests at the Pacific Proving Ground, fit Eq. (27) quite well.

The variation of Pacific nuclear events from Eq. (27) is primarily a yield dependent effect. This is illustrated in Figure 30 which is a plot of the ratio of observed $(R/d)^R_{HOB}$ to that calculated by Eq. (27). A straight line has been fit to the data with a standard deviation as indicated by the dashed lines. (The tank shots were ignored in the fit.)

The deviation of aspect ratios of Pacific events at higher yields is not a new result. Numerous explanations such as water washing[12], crater slumping[41], and dynamic liquification[13] have been offered. Any explanation should be consistent with the observed dependence,

$$(R/d)^R_{obs}/(R/d)^R_{pred} \propto Y^{1.15} \pm 0.5. \tag{28}$$

A completely empirical observation is noted which may, eventually, lead to a resolution of the wide scatter observed in Pacific nuclear crater dimensions. Events whose reduced aspect ratio is higher (lower) than the line in Figure 30 have larger (smaller) volumes than predicted from the line in Figure 27. This is clearly indicated in Figure 31. Since the deviations from Eq. (28) are strongly correlated with those from volume data, we must conclude that anomalies in shape and volume are due to a single cause.

If the shape factor F is plotted against scaled yield for the Ottawa sand tests shown in Table 6, a trend to higher F at higher scaled yield can be ascertained. Numerically, it is found that $F = (0.58 \pm 0.03) \ g^3 W/(U^6_\delta) \ ^{0.0045}$ Because of this slight yield dependence of F, the crater dimensions R and d do not quite scale as $V^{1/3}$. Rather, we have $(R,d) \propto W^{0.279} = W^{1/3.6}$.

One final point on crater shape factors (F) will be made. There is little

72
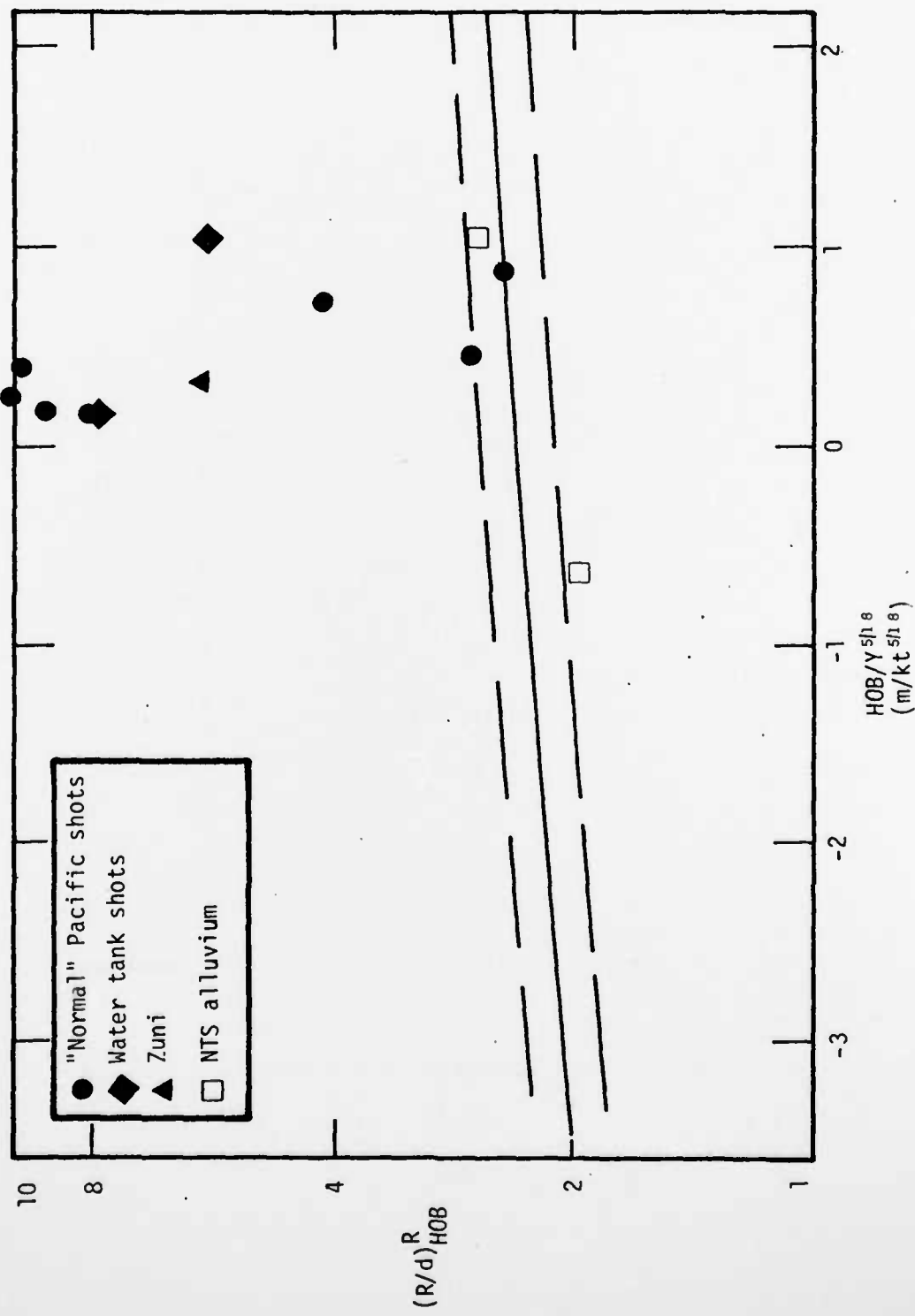
Figure 29. Reduced aspect ratio-scaled height of burst effects for nuclear tests.
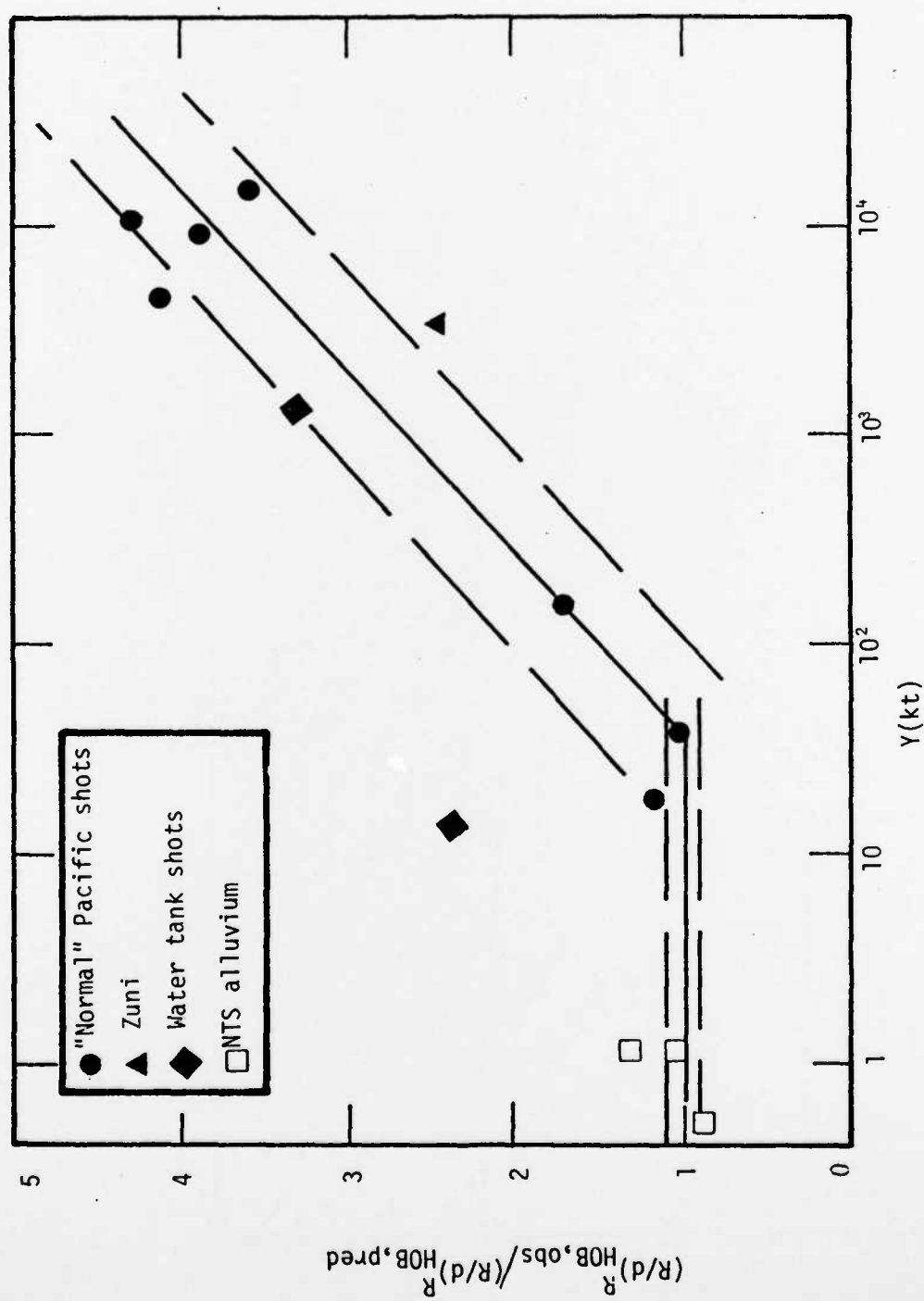
Figure 30. Yield dependence of deviation of R/d for Pacific events.
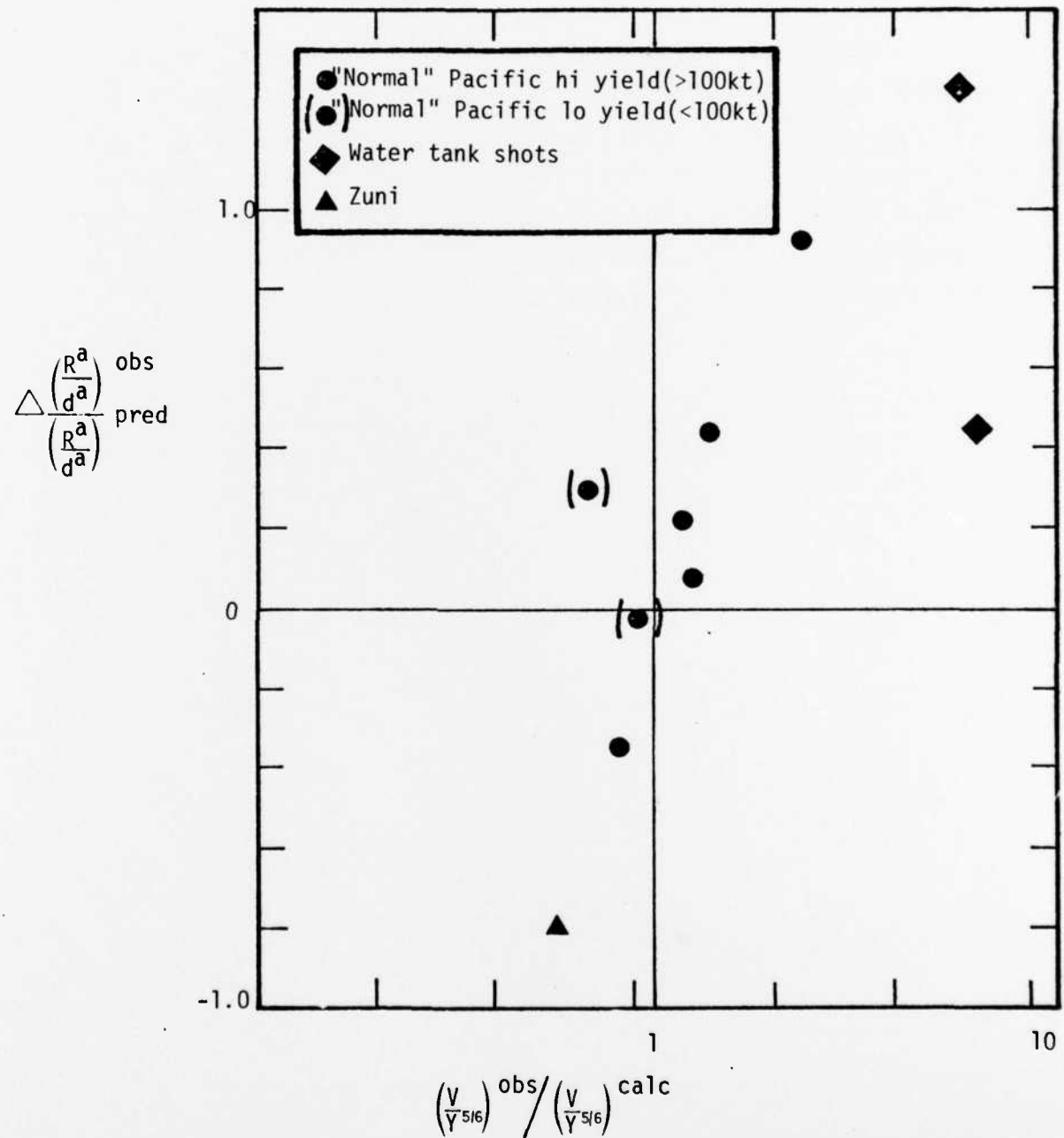
74

Figure 31.   Deviation of observed Pacific crater
volumes and aspect ratios from mean
values taken from Figures 27 and 30.

75

height of burst dependence of F seen in the PACE series, and values are similar to those of lower yield Pacific nuclear events, as well as JOHNIE BOY and JANGLE S (all are 0.5 ± 0.1 except SEMINOLE (a tank shot)) which has F = 0.67. However, events with yield over 100 kt have F = 0.26 ± 0.04, except for ZUNI and TEWA. ZUNI and TEWA exhibit the largest volume and aspect ratio anomaly (of the non-tank events) as well as being anomalous in F. However, a correlation similar to that shown in Figure 31 is not apparent.

5. REFERENCES

1.   Pokrovsky, G. I., "Diffusion Blasting: Coal Mining", Military Aeronautical Engineering Academy, Moscow, Priorada No. 8, pp. 81-83, 1957.

2.   Chabai, A. J., "Crater Scaling Laws for Desert Alluvium", SC-4391 (RR), Sandia Laboratories, 1959.

3.   Vaile, R. B., "Pacific Craters and Scaling Laws", Journal of Geophysical Research 66, No. 10, 1961.

4.   Violet, C. E., "A Generalized Empirical Analysis of Cratering", Journal of Geophysical Research 66, p. 3461 ff, 1961.

5.   Nordyke, M. D., "Nuclear Craters and Preliminary Theory of the Mechanics of Explosive Crater Formation", Journal of Geophysical Research 66, p. 3439 ff, 1961.

6.   Chabai, A. J., "On Scaling Dimensions of Craters Produced by Buried Explosives", Journal of Geophysical Research 70, No. 20, 1965.

7.   Dillon, L. A., "The Influence of Soil and Rock Properties on the Dimensions of Explosion-Produced Craters", AFWL-TR-71-144, Air Force Weapons Laboratory, 1972.

8.   Saxe, H. C. and Del Monzo, D. D., "A Study of Underground Explosion Cratering Phenomena in Desert Alluvium", Symposium on Engineering with Nuclear Explosives, 1970.

9.   Westine, P. S., "Explosive Cratering", J. Terramech. 7, 1970.

10.   Viktorov, V. V. and Stepnov, R. D., "Modeling of the Action of an Explosion with Concentrated Charges in Homogeneous Ground", Sandia Laboratories Translation SC-T-392, 1960.

11.   Johnson, S. W., et al., "Gravity and Atmospheric Pressure Effects on Crater Formation in Sand", Journal of Geophysical Research 74, No. 20, 1969.

12.   Vortman, L. J., "Craters from Surface Explosions and Scaling Laws", Journal of Geophysical Research 73, p. 4621 ff, 1968.

13.   Allen, R. T., "Crater Formation from High Explosive and Nuclear Surface Bursts", PT-U75-0030, Pacifica Technology, 1975.

14.   Knowles, C. P., "A Review of Energy Coupling from Nuclear Weapons", presented at the DNA Strategic Structures Review Meeting, Stanford Research Institute, February, 1975.

15.   Piekutowski, A. J., "A Comparison of Cratering Effects for Lead Azide and PETN Explosive Charges", AFWL-TR-74-182, Air Force Weapons Laboratory, 1975.

16.   McKay, M., et al., "Development and Preliminary Tests of a Cratering and Ground Motion Simulation Technique", DNA 3262F, Defense Nuclear Agency, 1974.

17.   Bucky, P. N., "Use of Models for the Study of Mining Problems", A. I. M. E. Tech. Pub. No. 425, pp. 3-28.

18.   Pokrovsky, G. I. and Boulytchev, V., "Soil Pressure Investigation on Sewers by Means of Models", Technical Physics of the USSR, Vol. I, No. 2, pp. 121-123, 1934.

19.   Pokrovsky, G. I. and Fyodorov, I., "Investigation by Means of Models of Stress Distribution in the Ground and the Setting (sic) of Foundations", Technical Physics of the USSR, Vol. II, No. 4, pp. 299-311, 1935.

20.   Pokrovsky, G. I. and Fyodorov, I., "Studies of Soil Pressures and Soil Deformations by Means of a Centrifuge", Proc. (1st) Int. Conf. on Soil Mechanics and Found. Eng., Vol. I, p. 70, 1936.

21.   Pokrovsky, G. I. and Fyodorov, I. S., Centrifugal Model Testing in the Construction Industry, Niedra Pub. House, Moscow, 1969.

22.   Ramberg, H., Gravity Deformation and the Earth's Crust, Academic Press, New York, 1967.

23.   Ramberg, H. and Sjostrom, H., "Experimental Geodynamical Models Relating to Continental Drift and Orogenesis", Tectonophysics, pp. 105-132, 1973.

24.   Schofield, A. N., "The Manchester Centrifuge Facility", Proc. 7th Int. Conf. on Soil Mech. and Found. Eng., 3, 536, 1969.

25.   Avgherinos, P. J., "Centrifugal Tests on Soil Models", Ph.D. Thesis, Cambridge, University, 1969.

26.   Avgherinos, P. J., and A. N. Schofield, "Drawdown Failures of Centrifuge Models", Proc. 7th Int. Conf. on Soil Mech. and Found. Eng., 2, 497-505, 1969.

27.   Rowe, P. W., "The Relevance of Soil Fabric to Site Investigation Practice", Geotechnique, Vol. 22, pp. 191-300, 1972.

28.   Roscoe, K. H., "Soils and Model Tests", Journal of Strain Analysis, Vol. 3, pp. 57-64, 1968.

29. Hoek, E., "The Design of a Centrifuge for the Simulation of Gravitational Force Fields in Mine Models", Journal of the South African Inst. of Mining and Metallurgy, vol. 65, pp. 455-487, no. 9, 1965.

30. Laut, P., "Application of Centrifugal Model Tests in Connexion with Studies of Flow Patterns of Contaminated Water in Soil Structure", Geotechnique, vol. 25, pp. 401-406, 1975.

31. Malushitsky, Y. N., The Stability of Slopes and Embankments (Centrifugal Model Testing), Budivelnik Pub. House, Kiev, 1975.

32. Mikasa, M. and Takada, No., "Significance of Centrifugal Model Test in Soil Mechanics", Proc. 8th Int. Conf. of Soil Mech. and Found. Eng., vol. 1.2, pp. 273-278.

33. Ovesen, N. Krebs, "Centrifugal Testing Applied to Bearing Capacity Problems of Footings on Sand", Geotechnique, vol. 25, pp. 394-401, 1975.

34. Al-Hussaini, M. M., "Centrifuge Model Testing of Soils: A Literature Review", Miscellaneous Paper S-76, 9 Waterways Experiment Station, 1976.

35. Herrmann, W., "On the Elastic Compression of Crushable Distended Materials", Sandia Development Report SC-DR-68-321, 1968.

36. Maxwell, D., et al., "JOHNIE BOY Crater Calculations", DNA 3048F, Defense Nuclear Agency, 1973.

37. Burton, D. E., et al., "Computer Design of High Explosive Experiments to Simulate Subsurface Nuclear Detonations", UCRL-75190, Lawrence Livermore Laboratory, 1973.

38. Maxwell, D. E., "Cratering Flow and Crater Prediction Methods", TCAM 73-17, Physics International, 1973.

39. Allen, R. T., "Equation of State of Rocks and Minerals", GAMD AMD-7834, General Atomics, 1967.

40. Exp. Chem. Sec., Gen. Chem. Div., "Properties of Chemical Explosives", UCRL-14592, Lawrence Radiation Laboratory, 1965.

41. Cooper, H. F., "Estimates of Crater Dimensions for Near Surface Explosions of Nuclear and High Explosive Sources", RDA-TR-2604-001, September 1976.

42. Lockard, D. M., "Crater Parameters and Material Properties", AFWL-TR-74-200, Air Force Weapons Laboratory, 1974.

43.   Schmidt, R. M. and K.A. Holsapple, "Centrifuge Cratering Experiments in Dry Granular Soils", Boeing Aerospace Co. Draft Final Report on Contract No. DNA 001-77-C-0169, 14 March 1977 - 31 January 1978.

44.   Schmidt, R. M., "A Centrifuge Cratering Experiment: Development of a Gravity Scaled Yield Parameter", in Impact and Explosion Cratering, D.J. Roddy, R.O. Peppin and R.B. Merrill (eds.), Proc. 8th Lunar Sci. Conf., Pergamon, New York, 1977.

45.   Fair, H. D. and Walker, R. F., Energetic Materials-I: Physics and Chemistry of Inorganic Azides, Plenum, New York, 1977.

DISTRIBUTION LIST

DEPARTMENT OF OEFENSE

Assistant to the Secretary of Defense
Atomic Energy
    ATTN: Executive Assistant

Defense Advanced Rsch. Proj. Agency
    ATTN: TIO
    ATTN: NMRO
    ATTN: PMO
    ATTN: STO

Defense Civil Preparedness Agency
Assistant Director for Research
    ATTN: Admin. Officer

Defense Documentation Center
Cameron Station
12 cy ATTN: TC

Defense Intelligence Agency
    ATTN: OT-1C
    ATTN: DB-4C, E. O'Farrell
    ATTN: DT-2
    ATTN: OB-4E

Oefense Nuclear Agency
    ATTN: DDST
 2 cy ATTN: SPSS
 4 cy ATTN: TITL

Department of Defense Explo. Safety Board
    ATTN: T. Zaker

Field Command
Oefense Nuclear Agency
    ATTN: FCT
    ATTN: FCTMOF
    ATTN: FCPR

Field Command Test Directorate
Test Construction Division
Oefense Nuclear Agency
    ATTN: FCTC

Interservice Nuclear Weapons School
    ATTN: Document Control

Joint Strat. Tgt. Planning Staff
    ATTN: NRI-STINFO, Library

Livermore Oivision, Field Command, ONA
Department of Defense
Lawrence Livermore Laboratory
    ATTN: FCPRL
    ATTN: L-200- J. Bryan
    ATTN: L-200, R. Swift
    ATTN: L-200, J. Thompson

Commandant
NATO School (SHAPE)
    ATTN: U.S. Documents Officer

Under Secretary of Defense for Rsch. & Engrg.
Oepartment of Defense
    ATTN: Strategic & Space Systems (OS)

DEPARTMENT OF DEFENSE (Continued)

WWMCSS System Engineering Organization
    ATTN: T. Neighbors

DEPARTMENT DF THE ARMY

BMD Advanced Technology Center
Huntsville Office
Department of the Army
    ATTN: 1CRDABH-X
    ATTN: CRDABH-S

Chief of Engineers
Department of the Army
    ATTN: DAEN-RDM
    ATTN: OAEN-MCE-D

Deputy Chief of Staff for Ops. & Plans
Department of the Army
    ATTN: MOCA-ADL

Deputy Chief of Staff for Rsch. Oev. & Acq.
Department of the Army
    ATTN: DAMA-AOA-M

Harry Diamond Laboratories
Oepartment of the Army
    ATTN: DELHO-NP
    ATTN: DELHD-TI

Redstone Scientific Information Ctr.
U.S. Army R&O Command
    ATTN: Chief, Documents

U.S. Army Ballistic Research Labs
    ATTN: Technical Library
    ATTN: DRXBR-X, J. Meszaros
    ATTN: DRDAR-BLE, J. Keefer
    ATTN: DRXBR-BLE, W. Taylor

U.S. Army Engineer Center
    ATTN: ATSEN-SY-L

U.S. Army Engineer Div., Huntsville
    ATTN: HNDED-SR

U.S. Army Engineer Div., Ohio River
    ATTN: ORDAS-L

U.S. Army Engr. Waterways Exper. Station
    ATTN: Library
    ATTN: G. Jackson
    ATTN: J. Strange
    ATTN: L. Ingram
    ATTN: W. Flathau

U.S. Army Materiel Mechanics Rsch. Ctr.
    ATTN: Technical Library

U.S. Army Materiel Oev. & Readiness Cmd.
    ATTN: DRXAM-TL

U.S. Army Mobility Equip. R&D Cmd.
    ATTN: OROME-WC

DEPARTMENT OF ENERGY (Continued)

Los Alamos Scientific Laboratory
ATTN: Doc. Con. for Reports Library
ATTN: Doc. Con. for G. Spillman
ATTN: Doc. Con. for R. Bridwell
ATTN: Doc. Con. for J-15
ATTN: Doc. Con. for TD-9

Oak Ridge National Laboratory
Union Carbide Corp.-Nuclear Division
ATTN: Doc. Con. for Technical Library
ATTN: Doc. Con. for Civil Def. Res. Proj.

Sandia Laboratories
Livermore Laboratory
ATTN: Doc. Con. for Library & Security
Classification Div.

Sandia Laboratories
ATTN: Doc. Con. for A. Chabai
ATTN: Doc. Con. for 3141

OTHER GOVERNMENT AGENCIES

Central Intelligence Agency
ATTN: RD/SI, Rm. 5G48, Hq. Bldg. for J. Ingley

Department of the Interior
Bureau of Mines
ATTN: Technical Library

National Science Foundation
Engineering Division
ATTN: C. Babendrier

Department of the Interior
U.S. Geological Survey
ATTN: D. Roddy

Department of the Interior
U.S. Geological Survey
ATTN: A. Moore

DEPARTMENT OF DEFENSE CONTRACTORS

Aerospace Corporation
ATTN: Technical Information Services

Agbabian Associates
ATTN: M. Agbabian

Applied Theory, Inc.
2 cy ATTN: J. Trulio

Avco Research & Systems Group
ATTN: Library, A830

Battelle Memorial Institute
ATTN: Library

BDM Corporation
ATTN: Corporate Library

Boeing Company
ATTN: Aerospace Library
ATTN: P. Schmidt
ATTN: K. Holsapple

Calspan Corporation
ATTN: Library

DEPARTMENT OF DEFENSE CONTRACTORS (Continued)

California Research & Technology, Inc.
ATTN: K. Kreyenhagen
ATTN: Library
ATTN: S. Shuster

Civil/Nuclear Systems Corporation
ATTN: R. Crawford
ATTN: J. Bratton

D. Gault
ATTN: D. Gault

California Institute of Technology
Jet Propulsion Laboratory
ATTN: H. Melosh
ATTN: R. Scott

University of Dayton
Industrial Security Super., KL-505
ATTN: H. Swift

University of Denver
Colorado Seminary
Denver Research Institute
ATTN: J. Wisotski

EG&G Washington Analytical Services Ctr., Inc.
ATTN: Library

Eric H. Wang
Civil Engineering Rsch. Fac.
ATTN: L. Bickle
ATTN: N. Baum

Gard, Incorporated
ATTN: G. Neidhardt

General Electric Company-TEMPO
Center for Advanced Studies
ATTN: DASIAC

IIT Research Institute
ATTN: Documents Library

Institute for Defense Analyses
ATTN: Classified Library

Kaman AviDyne
Division of Kaman Sciences Corporation
ATTN: E. Criscione
ATTN: Library

Kaman Sciences Corporation
ATTN: Library

Lockheed Missiles & Space Company, Inc.
ATTN: TIC-Library

Lockheed Missiles and Space Company, Inc.
ATTN: Technical Library
ATTN: Technical Information Center
ATTN: T. Geers

McDonnell Douglas Corporation
ATTN: R. Halprin

Merritt CASES, Inc.
ATTN: Library
ATTN: J. Merritt

DEPARTMENT OF DEFENSE CONTRACTORS (Continued)

Lockheed Electronics
        ATTN: R. Schaal

Nathan M. Newmark
Consulting Services
University of Illinois
        ATTN: N. Newmark

Pacifica Technology
        ATTN: J. Kent
        ATTN: R. Allen
        ATTN: E. Gaffney
        ATTN: R. Bjork

Physics International Company
        ATTN: F. Sauer
        ATTN: Technical Library
        ATTN: D. Orphal
        ATTN: R. Swift
        ATTN: E. Moore
        ATTN: L. Behrmann
        ATTN: C. Vincent

R&D Associates
        ATTN: C. MacDonald
        ATTN: H. Brode
        ATTN: A. Latter
        ATTN: Technical Information Center
        ATTN: C. Knowles
        ATTN: J. Carpenter
        ATTN: W. Wright, Jr.
        ATTN: J. Stockton
        ATTN: R. Port
        ATTN: J. Lewis

R&D Associates
        ATTN: H. Cooper

Science Applications, Inc.
        ATTN: Technical Library

Science Applications, Inc.
        ATTN: R. Shunk

Science Applications, Inc.
        ATTN: D. Maxwell
        ATTN: D. Bernstein

DEPARTMENT OF DEFENSE CONTRACTORS (Continued)

Southwest Research Institute
        ATTN: W. Baker
        ATTN: A. Wenzel

SRI International
        ATTN: B. Gasten
        ATTN: G. Abrahamson

Systems, Science & Software, Inc.
        ATTN: D. Grine
        ATTN: T. Riney
        ATTN: T. Cherry
        ATTN: Library

Terra Tek, Incorporated
        ATTN: Library
        ATTN: L. Hwang

Terra Tek, Incorporated
        ATTN: Library
        ATTN: S. Green

TRW Defense & Space Sys. Group
  2 cy ATTN: P. Dai
        ATTN: Technical Information Center
        ATTN: D. Baer
        ATTN: R. Plebuch
        ATTN: I. Alber

TRW Defense & Space Sys. Group
San Bernardino Operations
        ATTN: E. Wong

Universal Analytics, Inc.
        ATTN: E. Field

Weidlinger Assoc., Consulting Engineers
        ATTN: J. Wright
        ATTN: M. Baron

Weidlinger Assoc., Consulting Engineers
        ATTN: J. Isenberg

Westinghouse Electric Corporation
Marine Division
        ATTN: W. Volz

University of Dayton
        ATTN: A. Piekutowski

EN
DAT
FILM

tests shown in Table 6, a trend to higher F at higher scaled yield can be ascertained. Numerically, it is found that $F = (0.58 \pm 0.03)\ g^3 W/(U_\delta^6)\quad 0.0045$ Because of this slight yield dependence of F, the crater dimensions R and d do not quite scale as $V^{1/3}$. Rather, we have $(R,d) \propto W^{0.279} = W^{1/3.6}$.

One final point on crater shape factors (F) will be made. There is little

72

10

8

4

2

1

$(R/d)^R_{HOB}$

Figure

$(R/d)^R_{HOB}$

Figure 31. Deviation of observed Pacific crater volumes and aspect ratios from mean values taken from Figures 27 and 30.